Numerical investigations of the mantle plume initiation model for flood basalt events

Cinzia G. Farnetani and Mark A. Richards

Department of Geology and Geophysics, University of California, Berkeley

Abstract. Recent studies have linked both the eruption of continental flood basalts and the emplacement of large oceanic plateaus to the initial phase of mantle plume activity, i.e., the "plume head" model. Here we develop this concept further through numerical models of a large thermal diapir rising through the mantle and impinging upon the base of the lithosphere. A finite element analysis in axisymmetric geometry is used to model the dynamics of solid state convective flow and heat transport in the mantle, and an anhydrous batch melting model is used to estimate melt volumes and compositions obtained from partial melting in the shallow mantle. We explore the effects of a number of model variables, including mantle viscosity structure, plume temperature and diameter, and the mechanical response of the lithosphere. Our study emphasizes cases in which the lithosphere does not undergo significant extension prior to large-scale melting. A "standard model" is found to be consistent with some observed characteristics of flood basalt/plume initiation events. This model includes an initial diapir of radius 400 km and initial excess temperature 350°C rising through a mantle of viscosity ~10^{21}Pa s and impinging beneath a model oceanic lithosphere ~100 Ma in age. If lithospheric extension does not occur, melting is almost entirely sublithospheric; the melt volume produced is ~3.5×10^6 km^3 and its composition has high MgO content (15-20 wt %). A time sequence of precursory central (axial) uplift of several kilometers followed by major melting (volcanism) is a robust feature of all the models, regardless of mantle viscosity structure or lithospheric response. Low viscosity in the upper mantle compresses the timescale for these events, and results in a constriction of the plume "head" initially impinging on the lithosphere. The radial extent of the melting region (about 500 km at the time of maximum melt production) is only slightly affected by the upper mantle viscosity. For nonrifting lithosphere, no significant melt generation occurs for initial plume excess temperatures less than about 300°C. The initial plume radius has only a modest effect upon the volume of melt obtained. The most important aspect of lithospheric response is whether or not the uppermost crust and lithosphere (above ~40 km depth) undergo extension: otherwise, the ductile strength of the lower lithosphere has little effect. If the lithosphere is allowed to extend freely, the melt volume increases by about an order of magnitude, and it is comparable with some of the largest oceanic plateaus such as Ontong Java. If continental or oceanic flood basalt events occur on old, nonrifting lithosphere, the primary melts are likely to be much more MgO rich than the basalts erupted at the surface. This is consistent with abundant evidence for olivine fractionation in many flood basalt provinces, along with the occurrence of picrite lavas, and we hypothesize that fractionation occurs at a density trap at the crust/mantle boundary (Moho). At this stage and following, it is likely that significant lower crustal and mantle-lithospheric contamination of mantle plume-derived magmas may occur, both isotopically and in the trace elements. The sequence and timing of both precursory and post-magmatic events in the vast, well-exposed oceanic flood basalt terrane known as "Wrangellia" (SE Alaska; British Columbia) are consistent with the predictions of our model. The uplift predicted by our models is of order 2-4 km if we require that mantle plumes are hot enough to melt beneath unrifted lithosphere. Effects not modeled here, such as small-scale convection and hydrous melting, will tend to reduce the model excess temperature and uplift. In order to better understand the relation between mantle plumes and large igneous provinces, several important advances are required: implementation of a fractional melting model, some realistic assessment of melt transport through the mantle and crust, and a fully three-dimensional convection model.

Introduction

Flood basalt eruptions are extraordinary volcanic events which give rise, literally, to floods of basaltic lava that cover vast areas of the Earth's surface very rapidly. These events are

not explained by normal plate tectonic activity at convergent or divergent margins, and they occur in a variety of tectonic settings [*Hill et al.,* 1992]. Continental flood basalts are commonly associated with lithospheric rifting and continental break-up [*White and McKenzie,* 1989], although major crustal extension does not appear to be required for flood volcanism [*Richards et al.,* 1989; *Hooper,* 1990].

Estimated extruded volumes for the largest flood basalt events such as the Karoo, the Deccan traps, the Paraná-

Etendeka, the Siberian traps, and the North Atlantic Province, (Figure 1) are of order 1 or 2×10^6 km³ [*Richards et al.*, 1989], with perhaps similar (but unknown) volumes of intrusive magmatism. Recent estimates of total melt volumes for the Deccan and the North Atlantic Province are of order 6 and 8×10^6 km³, respectively [*Coffin and Eldholm*, 1993, 1994]. All these provinces typically cover areas ~1000-2000 km in radius [*White and McKenzie*, 1989], although the loci for eruptions may be more confined. Magnetostratigraphic and radiometric age data indicate that the bulk of the volcanic activity occurs in just a few million years, yielding eruption rates of ~1 km³/yr, or greater [e.g., *Richards et al.*, 1989; *Renne et al.*, 1992; *Coffin and Eldholm*, 1994]. Flood basalt events are generally preceded by a period of thermal doming and uplift of order ~2 km [e.g., *Cox*, 1989], although the timing and duration of uplift are often difficult to constrain.

Large volcanic oceanic plateaus are also likely to have resulted from flood volcanism [*Richards et al.*, 1991], and estimated volumes for some plateaus are very large indeed: at least a few million cubic kilometers for the Caribbean Plateau; for the Kerguelen Plateau the extrusive component is $\sim 8 \times 10^6$ km³; and the estimated total volume is $\sim 10\text{-}15 \times 10^6$ km³ [*Coffin and Eldholm*, 1994]; for the Ontong Java Plateau the estimated total volume ranges from 30 to 60×10^6 km³ [*Coffin and Eldholm*, 1994]. Recent dating suggests that the bulk of the Ontong Java Plateau was erupted in just a few (~2-5) million years [*Tarduno et al.*, 1991; *Mahoney et al.*, 1993], in which case the eruption rates would be comparable to or larger than those for continental flood basalts. There is also evidence that oceanic plateau formation is accompanied by regional uplift of the ocean floor [*Richards et al.*, 1991].

Morgan [1972, 1981] noted the association of presently active hotspots with flood basalts and proposed that flood basalts occurred at the initiation of mantle plume activity. *Richards et al.* [1989] discussed eight such pairings in the Phanerozoic, noting that flood basalts typically erupt at rates an order of magnitude higher than associated continuous ("normal") hotspot track volcanism. According to the mantle plume initiation model [*Richards et al.*, 1989; *Campbell and Griffiths*, 1990; *Griffiths and Campbell*, 1990] the first massive volcanic event corresponds to melting of the large leading diapir, or "head", of the plume, while the following magmatic activity of the hotspot is associated with the remaining plume conduit, or "tail". In this model, lithospheric rifting may occur before, during, or after the main phase of volcanism, but it is not required.

An alternative proposed for the origin of flood basalts is the rifting/decompression model [*Morgan*, 1981; *White and McKenzie*, 1989], in which abnormally hot asthenosphere (associated with a mantle plume) wells up in passive response to continental stretching and rifting. This model seeks to explain the occurrence of flood basalts in association with continental rifting and has not been applied to oceanic plateau genesis. The passive rifting and plume initiation models share the common feature of mantle plume activity, but they differ markedly as to the role of the lithosphere. Clearly, lithospheric extension has a major effect on melt generation [*McKenzie and Bickle*, 1988], so the question is mainly one of geological observation: Is flood volcanism always preceded by major lithospheric extension? We have argued in the past [*Richards et al.*, 1989, 1991], as have others [*Hooper*, 1990; *Hill et al.*, 1992; *Heaman et al.*, 1992], that lithospheric
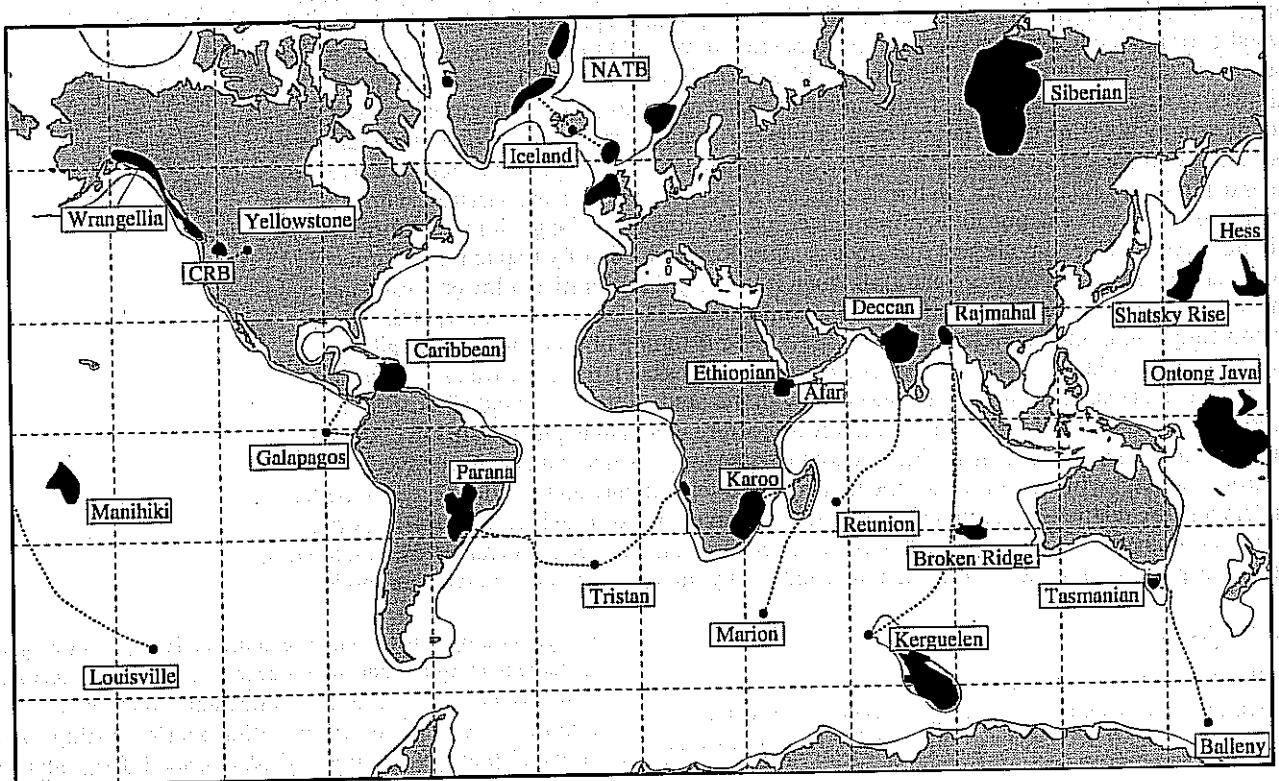

Figure 1. Schematic map showing selected flood basalt provinces and oceanic plateaus. The associated hotspots, where known or conjectured, are indicated. (Adopted from *Duncan and Richards* [1991]. For a more complete map of large igneous provinces, see *Coffin and Eldholm* [1994].)

extension is not required. We will not repeat those arguments here, but the matter is not yet resolved and remains a legitimate point for debate.

Important questions also remain concerning the specific predictions of the theoretical models. The plume initiation model has been developed on the basis of results from simple laboratory fluid dynamical experiments [*Whitehead and Luther*, 1975; *Olson and Nam*, 1986; *Griffiths and Campbell*, 1990], which show that hot, low-viscosity mantle plumes will develop a very large leading diapir, followed by a narrow conduit if the plume remains connected to its source. These models have been extremely useful, both qualitatively and quantitatively, but they do not address some important aspects of plume dynamics. In particular, they cannot be applied directly to partial melting processes, nor can they be used to understand important physical effects arising from variations in the mechanical properties of the deep mantle and lithosphere. Such aspects instead can be better elucidated by numerical models.

In this paper we present the results of numerical modeling of ascending large mantle diapirs in order to develop a broader range of quantitative, testable hypotheses from the plume initiation concept. Our finite element model in cylindrical axisymmetric geometry combines the dynamics of solid state convection in the mantle with a melting model. We start with a hot, spherical diapir in the lower mantle and follow its evolution as it rises through the mantle and spreads beneath the lithosphere. We calculate the history of surface uplift and mantle melting due to the hot plume head. We implement the empirical batch melting model of *McKenzie and Bickle* [1988] to estimate the total melt volume, the melt production rate, and the melt composition. We can investigate how parameters such as the melt volume, its primary composition, the amount and timing of uplift, etc., are functions of (1) buoyancy of the thermal diapir (which depends on its initial size and excess temperature), (2) different mantle viscosity structures, and (3) mechanical behavior of the lithosphere. The further step, which is to compare the results of the numerical model to the corresponding parameters observed or inferred in flood basalt provinces, can be done only at a very speculative level due to the simplicity of our model. The equilibrium melting model does not account for the compositional evolution of the residuum as melting proceeds and how this affects the melt fraction and its composition. Moreover, we do not model melt extraction, nor do we model attendant effects such as pressure changes resulting from melt extraction [*White et al.*, 1992] and heat transfer between the rising magma and the lithosphere. We also ignore the effect of volatile components, since the batch melting parameterization is based on anhydrous melting experiments. This last restriction may be particularly important in addressing the trace element and isotopic characteristics of continental flood basalts [*Gallagher and Hawkesworth*, 1992].

We choose to concentrate on the case of a mantle starting plume impinging on nonrifting oceanic lithosphere. There are several reasons for this: First, the composition and thermal structure of oceanic lithosphere are rather well-understood compared to continental lithosphere. Second, as will be shown below, the case of old, nonrifting lithosphere constitutes the most stringent test for the plume initiation model, especially with respect to melt production. We believe that the field evidence shows that at least some mantle plumes must be hot enough to melt without lithospheric extension.

Third, we are particularly interested in applications to the flood basalt formation in the Triassic strata of the famous Wrangellia terrain of Alaska and Vancouver Island, British Columbia. This accreted oceanic plateau contains a remarkable stratigraphic record of prevolcanic and postvolcanic events [*Richards et al.*, 1991], and the field evidence shows that flood volcanism occurred on old oceanic lithosphere without major crustal extension.

Numerical Methods

Finite Element Model

We use a finite element code (ConManCYL) for thermal convection within the Earth's mantle in cylindrical axisymmetric geometry. We have substantially modified the original Cartesian version of the code (ConMan, written by A. Raefsky and S. King) to satisfy the cylindrical geometry. The code solves the advection-diffusion equations for a Newtonian, incompressible and compositionally homogeneous viscous fluid. In nondimensional form the equations are

Incompressibility

$$\nabla \bullet U = 0 \tag{1}$$

Conservation of momentum for a fluid at infinite Prandtl number

$$-\nabla p + \nabla^2 U + RaT\hat{z} = 0 \tag{2}$$

Conservation of energy

$$\frac{\partial T}{\partial t} + (\nabla T) \bullet U = \nabla^2 T \tag{3}$$

where U is the velocity vector, T is the temperature, p is the dynamic pressure, t is time, Ra is the Rayleigh number, and $\hat{z}$ is a unit vector in the vertical direction. The equations are non-dimensionalized by scaling distance according to the cylinder depth d, temperature according to the temperature contrast δT across the lithosphere, and time according to d^2/κ, where κ is the thermal diffusivity. Numerical values of the scaling parameters are given in Table 1. All the material properties are combined in the Rayleigh number:

$$Ra = \frac{g\alpha\delta T d^3 \rho}{\kappa\eta} \tag{4}$$

where g is the gravitational acceleration, α is the coefficient of thermal expansion, κ is the thermal diffusivity, and ρ is the density. In our models the Rayleigh number becomes effectively a measure of mantle reference viscosity, and in (4), η is the viscosity of the lower mantle. Density variations due to temperature changes are neglected except in the calculation of the buoyancy forces (Boussinesq approximation).

The incompressibility equation is used to constrain the momentum equation by means of a penalty function formulation [*Hughes et al.*, 1979]. *Hughes* [1980] shows that in order to achieve correct results using the penalty formulation in the axisymmetric case a mean-dilatational approach ($\bar{B}$ method) must be applied to the stiffness matrix of the momentum equation. The momentum equation is solved using a Galerkin method and bilinear shape functions, and we apply the $\bar{B}$ method in its complete formulation [*Hughes,*

Table 1. Model Parameters and Physical Constants

Symbol	Model Parameters and Physical Constants	Values
d	dimensional depth of the cylinder	2600 km
δT	potential temperature contrast across the lithosphere	1280°C
g	gravitational acceleration	10 m s^{-2}
α	thermal expansion coefficient	3x10^{-5} °C^{-1}
ρ	mantle density	3500 kg m^{-3}
κ	thermal diffusivity	10^{-6} m^2 s^{-1}
C_p	specific heat at constant pressure	1200 J kg^{-1} °K^{-1}

1987]. The accuracy of the solutions for the velocity components has been checked against analytical solutions, calculated with a propagator matrix technique in cylindrical geometry [*Richards*, 1986]. The error is defined as $\varepsilon = (U_C - U_A) \times 100/U_A$, where U_C is the finite element value of the velocity component at each node and U_A is the corresponding analytical value. On a 66x66 test grid we achieved an $\varepsilon \leq 0.01\%$, with errors scaling as the square of the grid spacing.

The energy equation is solved using a streamline-upwind Petrov-Galerkin formulation since it is more accurate for advection dominated flows [*Brooks and Hughes*, 1982]. The time stepping in the energy equation is done using an explicit predictor-corrector algorithm, and the time step corresponds to the Courant time step [*King et al.*, 1990]. For a given temperature field the code calculates the corresponding velocity field, which is then used to advect the temperatures for the next time step and solve for a new temperature field.

The code uses an Eulerian grid of rectangular elements. In most of the models we present the size of the box is 1560 km in radius by 2600 km in depth, and we use a nonuniform grid with 70x120 elements (Figure 2). The height of each element is 13.8 km (from the surface to 200 km depth), 18.5 km (from 200 to 1000 km depth), and 26.0 km for greater depths. For radial distances less than 760 km the width of each element is 18.5 km, elsewhere the width is 27.8 km.

At the surface we impose zero vertical velocity ($U_z = 0$). For cases in which lithospheric extension is not allowed the radial component of the velocity is set to zero from the surface to a depth between 20 and 40 km, depending on the type of lithosphere (old or young) being modeled. On the bottom boundary we impose zero vertical velocity and radial free slip ($U_z = 0 = \partial U_r / \partial z$); while along the axis of symmetry and the right side of the box, we impose zero radial velocity and vertical free slip ($U_r = 0 = \partial U_z / \partial r$).

In the initial temperature configuration the mantle has a uniform potential temperature $T_m = 1280°C$, all boundaries are insulated except the top surface, which is assigned a constant temperature $T_{su} = 0°C$. The initial temperature profile for the oceanic lithosphere is given by an error function conduction profile corresponding to the appropriate age. The spherical thermal diapir, initially centered at 2000 km depth, is characterized by an initial excess potential temperature with respect to the mantle, ΔT_0, and by its radius, R_0. To avoid high-temperature gradients between the boundary of the thermal diapir and the surrounding mantle, we impose a "thermal halo", 130 km thick, in which the temperature decreases as a sine function with distance from the surface of the diapir. A "thermal halo" would develop anyway by diffusion, but by imposing it we avoid numerical instabilities

that may arise because of initially high temperature gradients. When calculating the initial radius of the diapir, we take into account the buoyancy induced by the thermal halo, so that R_0 should be considered an "effective" initial radius.

Uplift Calculations

Given the velocity components at each time step, we calculate the topographic uplift induced by the rising thermal diapir. In cylindrical geometry the vertical normal stress is

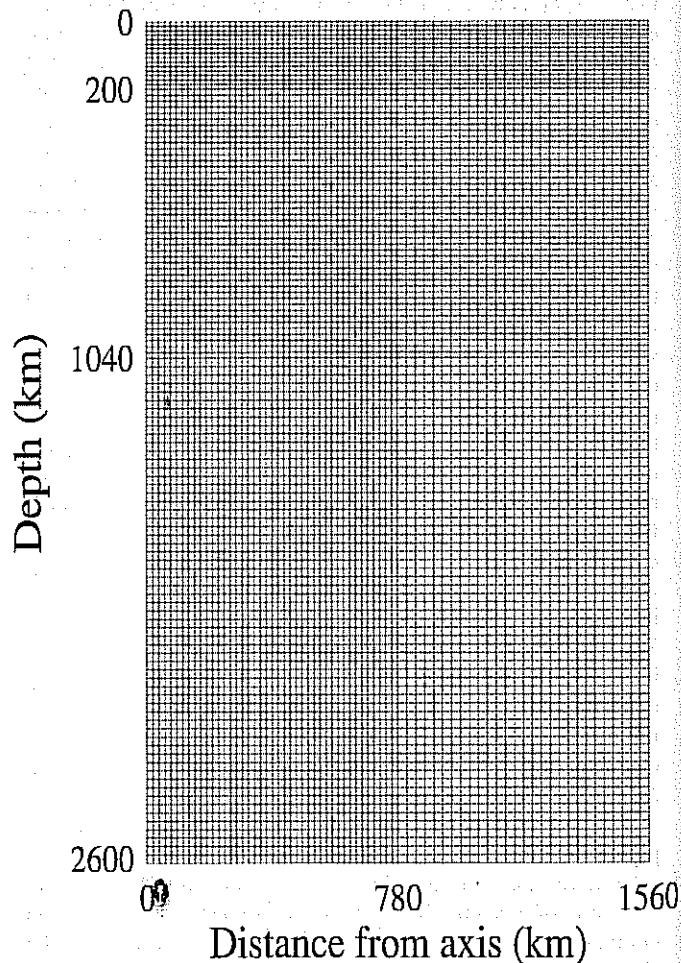$$\tau_{zz} = 2\eta \frac{\partial U_z}{\partial z} - p \qquad (5)$$

Figure 2. The standard finite element grid (70x120 elements). The left side is the axis of symmetry. The radius of the cylinder is 1560 km, and the depth is 2600 km. Note the higher resolution from the surface to 200 km depth.

where η is the viscosity and p is the dynamic pressure given by

$$p = -\lambda \nabla \cdot U \qquad (6)$$

where $\lambda = 10^7$ is the penalty parameter.

For each element we calculate the nondimensional average value of τ_{zz} which is assigned to the center of mass of each element. Values of τ_{zz} have also been checked against analytical solutions calculated with the propagator matrix technique. The error $\varepsilon = (\tau_{zzC} - \tau_{zzA}) \times 100/\tau_{zzA}$, where τ_{zzC} is the finite element value and τ_{zzA} is the corresponding analytical value, is $\varepsilon \leq 0.1\%$ on a 66x66 grid. The element τ_{zz} values are projected to the nodes using a modified version of the pressure-smoothing technique [*Hughes et al.*, 1979]. We dimensionalize τ_{zz} by multiplying it by $\rho g d \alpha \delta T / Ra$ and calculate the surface topographic uplift δh:

$$\delta h = \frac{(\tau_{zz} - \bar{\tau}_{zz})}{\rho_{su} g} \qquad (7)$$

where $\bar{\tau}_{zz}$ is the area-averaged value of the vertical normal stress at the surface and ρ_{su} is the effective density contrast at the upper surface. For continental lithosphere, ρ_{su} equals the mantle density ρ_m (both crust and mantle material are uplifted), while for oceanic lithosphere, $\rho_{su} = \rho_m - \rho_w$, where ρ_w is the density of seawater ($\rho_w = 1000$ kg m^{-3}).

Calculations of melt volume and composition

As the head of the thermal diapir spreads beneath the lithosphere, we estimate the total melt volume produced and its composition. We use a batch melting model, thus assuming that the liquid remains in chemical equilibrium with the solid residue until mechanical conditions allow it to escape as a single "batch" of primary magma. The requirement that no relative movement occurs between the melt and the matrix is probably unrealistic whenever the melt fraction exceeds 1 or 2% [*McKenzie*, 1984], and this will affect the total melt volume and its composition [*McKenzie and Bickle*, 1988]. We do not attempt to model melt extraction and its effect on the dynamics of the plume head and of the lithosphere, nor do we include directly the effect of melt buoyancy. Though it would be desirable to use a more realistic model for partial melting of a complex mineral assemblage, such as Rayleigh melting, the parameterization available is based on laboratory experiments which involve batch melting.

In this study we implement the parametrization by *McKenzie and Bickle* [1988] of batch melting experiments on garnet peridotite. We calculate the melt fraction and its composition at each time step for depths shallower than 220 km (i.e., from 0 to ~7 GPa, which correspond to the pressure range of *McKenzie and Bickle's* [1988] parameterization). As discussed below, this does not seem to be a limitation, since melting never occurs deeper than 150 km (i.e., ~5 GPa) in any of our model cases. We first convert the dimensional potential temperatures T_p to real temperatures T_r assuming an adiabatic gradient and using $T_p = T_r \times \exp(-g \alpha z / C_p)$, where z is the dimensional depth. The numerical value of C_p is given in Table 1. We calculate the lithostatic pressure P (in gigapascals) using the Preliminary Reference Earth Model (PREM) [*Dziewonski and Anderson*, 1981]. The solidus temperature (in degree Celsius) is obtained by numerical solution of

$$P = (T_s - 1100)/136 + 4.968 \times 10^{-4} \exp(1.2 \times 10^{-2}(T_s - 1100)) \quad (8)$$

while the liquidus temperature (in degree Celsius) is given by

$$T_l = 1736.2 + 4.343P + 180 \tan^{-1}(P/2.2169). \qquad (9)$$

The melt fraction X is expressed through a dimensionless temperature T':

$$T' = \frac{T_r - (T_l + T_s)/2}{(T_l - T_s)} \qquad (10)$$

by requiring that $X=0$ when $T_r = T_s$ and $X=1$ when $T_r = T_l$. The melt fraction at the center of each element is calculated using the empirical expression

$$X - 0.5 = T' + (T'^2 - 0.25)(a + bT') \qquad (11)$$

with the coefficients $a=0.4256$ and $b=2.988$. We also account for the change in temperature due to the latent heat of melting. At constant pressure the change in temperature dT due to a change in melt fraction dX is

$$dT = \Delta H \times dX/C_p \qquad (12)$$

for a reversible process the latent heat of melting ΔH is $\Delta H = \Delta S \times T_r$; thus

$$dT = \Delta S \times T_r \times dX/C_p. \qquad (13)$$

We assume that melting occurs at constant entropy of fusion ($\Delta S = 250$ J kg^{-1} °K^{-1}, as in *McKenzie and Bickle's* [1988] parameterization) and calculate the relation between melt fraction, temperature, and pressure using the equations in Appendix D of *McKenzie* [1984], where a fourth-order Runge-Kutta scheme is used to integrate the expressions relating X, T, P at constant ΔS. The values of the real temperature, modified by the latent heat of melting, are then converted back to dimensionless potential temperatures and used in the diffusion (conduction) term of the energy equation for the next time step.

The melt fraction by weight X is related to the volume fraction of melt ϕ through

$$\phi = \frac{X \rho_s}{\rho_f + X(\rho_s - \rho_f)} \qquad (14)$$

and we assume that the density of the solid ρ_s and the density of the melt ρ_f are equal. The total melt volume is then obtained by integration of the volume fraction of melt of each element over the entire melting region. We calculate the point average composition of the melt in terms of the major element oxides using the *McKenzie and Bickle* [1988] parameterization. The values obtained are probably only indicative, since the method has some limitations when melting occurs at high pressure [*Watson and McKenzie*, 1991].

The Model

Thermal Diapir

We assume that mantle plumes originate from a hot boundary layer in the mantle, possibly the core-mantle boundary (CMB). Laboratory experiments [*Whitehead and*

Luther, 1975; *Campbell and Griffiths*, 1990] show that a newly formed thermal plume develops a large "head" and a "tail". The head forms since a large amount of buoyancy is needed before the plume is able to displace the overlying colder fluid and rise. The "tail" of thermal plumes is maintained by continued buoyancy flux from the bottom boundary. This tail is a somewhat arbitrary feature of the fluid dynamical experiments, since a constant buoyancy flux is imposed. Natural boundary layer instabilities arising in free convection may or may not be continuously fed from the boundary layer, depending on the particular conditions.

In the mantle plume initiation model, flood basalts are generated by melting of the head of the plume [*Morgan*, 1981; *Richards et al.*, 1989; *Campbell and Griffiths*, 1990], and in this first phase the contribution of the material rising through the tail is of secondary importance. Given the uncertainties in the details of how thermal instabilities would form at the CMB, we simply consider a hot, spherical diapir placed initially at 2000 km depth, which is not connected to any boundary layer. By doing this we avoid numerical modeling difficulties in resolving the tail, especially for the very thin conduits that would result in cases with strongly temperature dependent viscosity. The buoyancy of the thermal diapir is proportional to the excess temperature with respect to the mantle and to the cube of its radius. We investigate a range of initial radii $300 \le R_0 \le 500$ km and initial excess temperatures $300 \le \Delta T_0 \le 400°C$. The initial excess temperature ΔT_0 is expected to be higher than the excess temperature (ΔT) estimated from petrologic constraints. The excess temperature that best fits the Hawaii hotspot swell is 200-300°C [*Sleep*, 1990], in agreement with a plume temperature of ~1500°C for magma generation beneath Hawaii [*Wyllie*, 1988]. The range of initial radius values we model is consistent with values estimated from laboratory experiments [*Campbell and Griffiths*, 1990] scaled to mantle conditions.

Mantle Viscosity Structure

Laboratory experiments have investigated the rise of a plume in a uniform viscosity fluid, but numerical modeling can address the effect of more realistic viscosity structures. Geophysical studies indicate that mantle viscosity may increase from the upper to the lower mantle by 1 or 2 orders of magnitude [e.g., *Hager*, 1984; *Nakada and Lambeck*, 1990]. Viscosity may change discontinuously at depth where phase changes occur, and it might vary continuously with depth due to the effects of pressure on the rheology of mantle materials.

We consider several viscosity structures and some temperature dependent viscosity cases. (We do not attempt to model other thermodynamical effects of phase changes.) In this study the values of the lower mantle viscosity (η_{lm}) range from 3×10^{22} to 3×10^{21} Pa s, and for the upper mantle viscosity (η_{um}) values range from 3×10^{21} to 3×10^{19} Pa s. This covers a reasonable range of mantle viscosities, though more extreme values are possible. The uniform mantle viscosity model has $\eta=10^{21}$ Pa s. Figure 3 shows the viscosity profiles for the "standard" model ($\eta_{lm}=10^{22}$ Pa s) for viscosity contrasts of $\gamma=10$ and $\gamma=100$ ($\gamma= \eta_{lm}/ \eta_{um}$). The change in viscosity between the lower and upper mantle is at 670 km depth. The stiff rheology of the lithosphere is modeled by an increase in uppermost mantle viscosity up to 10^{22} Pa s (see next section). For temperature dependent viscosity we adopt the following exponential dependence:

$$\eta(T) = \eta_0 \exp(-4.60T) \qquad (15)$$

which gives two orders of magnitude viscosity contrast across the lithosphere.

Lithosphere

The lithosphere is modeled by imposing an initial temperature profile and a viscosity structure (note that we concentrate on oceanic lithosphere for the reasons stated in the introduction). The initial temperature profile is given by an error function conduction profile [*Parson and Sclater*, 1977] according to the initial age. We investigate initial ages 0 Ma, 20 Ma, and 100 Ma. For nontemperature dependent viscosity cases, the viscosity of the lithosphere is 10^{22} Pa s from the surface to 55 km depth (for 100 Ma old lithosphere), or to 41 km depth (for 20 Ma and 0 Ma lithosphere). The viscosity decreases smoothly below these depths to upper mantle viscosity values (Figure 3). For a given initial age the viscosity structure of the uppermost 80 km is kept constant, independent of the values of the upper mantle viscosity (except for cases with temperature dependent viscosity). We note that these lithospheric viscosities are rather modest, so that we are generally modeling "best case" scenarios for melting due to the rise of hot plume material into the lower lithosphere.
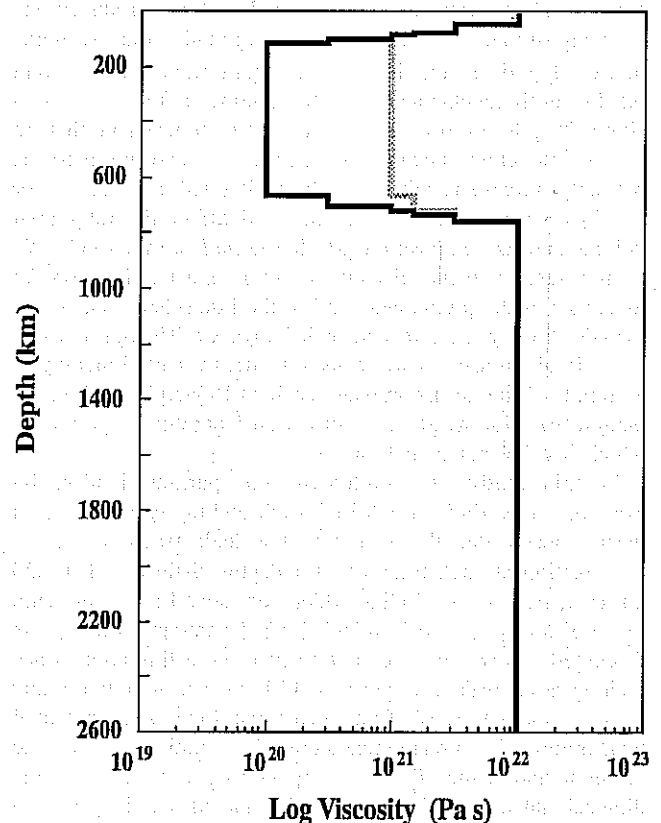
Viscosity Models

Figure 3. Mantle viscosity profiles for the two standard models: $\gamma=10$ (thin line) and $\gamma=100$ (thick line). $\gamma= \eta_{lm}/ \eta_{um}$ is the ratio of lower mantle viscosity (η_{lm}) and upper mantle viscosity (η_{um}).

We also investigate the effects of lithospheric extension. If extension is allowed, we simply use a free radial slip boundary condition at the top surface nodes of the finite element grid. This allows extension to occur naturally since all internal nodes are unconstrained. For the majority of cases in which extension is not allowed, we impose zero radial velocity from the surface to 40 km depth for an initial age of 100 Ma, or to 28 km depth for 20 Ma lithosphere. It is important to note that the axisymmetry of our calculations requires that any horizontal extension be radial, so that we cannot generate more realistic models with unidirectional extension (rifting) of the lithosphere.

Results

The numerical model described above allows us to investigate the evolution of a thermal diapir as it rises in the mantle and impinges on oceanic lithosphere. We calculate the temporal and spatial variations of the surface uplift, the radial deviatoric (extensional) stress induced in the lithosphere, and the total melt volume. The model parameters vary about a "standard" case in which the thermal diapir has an initial excess potential temperature $\Delta T_0 = 350°C$, an initial radius $R_0 = 400$ km, the lower and upper mantle viscosities are $\eta_{lm} = 10^{22}$ Pa s and $\eta_{um} = 10^{21}$ Pa s, respectively ($\gamma = 10$), the lithosphere is nonrifting and its initial age is 100 Ma. Figure 4 shows the time evolution of the thermal diapir for this standard model, starting from the initial condition (Figure 4a). After 20 m.y. (Figure 4b) the head of the diapir is at 670 km depth, while after 30 m.y. (Figure 4c) the plume head is at 180 km depth. Just prior to sublithospheric spreading the plume radius is ~350 km. Melting starts at 34 m.y. and increases as the plume head spreads beneath the lithosphere. The melting

region (for melt fraction $X > 0\%$) is indicated in Figure 4d by the white area beneath the lithosphere. The maximum melt production occurs after 45 m.y. and the total melt volume produced is 3.7×10^6 km^3. At this time the radius of the plume head is ~700 km and the radius of the melting region for melt fraction $X > 5\%$ is ~580 km. Melting occurs at sublithospheric depths (100-150 km) since not enough time has elapsed for conductive heating the lithosphere above the solidus.

Figure 5 shows the time evolution of the initial diapir (Figure 5a) if the upper mantle viscosity is reduced to $\eta_{um} = 10^{20}$ Pa s ($\gamma = 100$) in the standard model. After 20 m.y. (Figure 5b) the head of the diapir is at 670 km depth. As it enters the upper mantle, a narrow conduit develops (with radius ~100 km) through which the hot material ascends at higher velocity, so that after only 24 m.y. (Figure 5c) the plume head is at ~180 km depth. The narrowing effect reduces the radius of the plume head impinging on the lithosphere to ~150 km. Melting starts after 24 m.y. and reaches a maximum after 33 m.y. (Figure 5d), the total melt volume produced is 2.6×10^6 km^3. The radius of the plume head at this time is ~620 km, while the radius of the melting region, for melt fraction $X > 5\%$, is ~360 km. The "narrowing" of the plume head is a consequence of the velocity increase of the buoyant fluid when it enters a lower-viscosity material [e.g., see *Richards et al.,* 1988]. The above figures illustrate that the viscosity structure of the mantle affects the dynamics of a rising plume and that 2 orders of magnitude viscosity contrast between the lower and upper mantle causes pronounced "necking". This ultimately influences the shape and size of the plume head and the radial extent of the melting zone.

For comparison, Figure 6 shows the evolution of the standard diapir (ΔT_0 and R_0 as above) rising in a uniform viscosity mantle ($\eta = 10^{21}$ Pa s). No necking occurs, and the
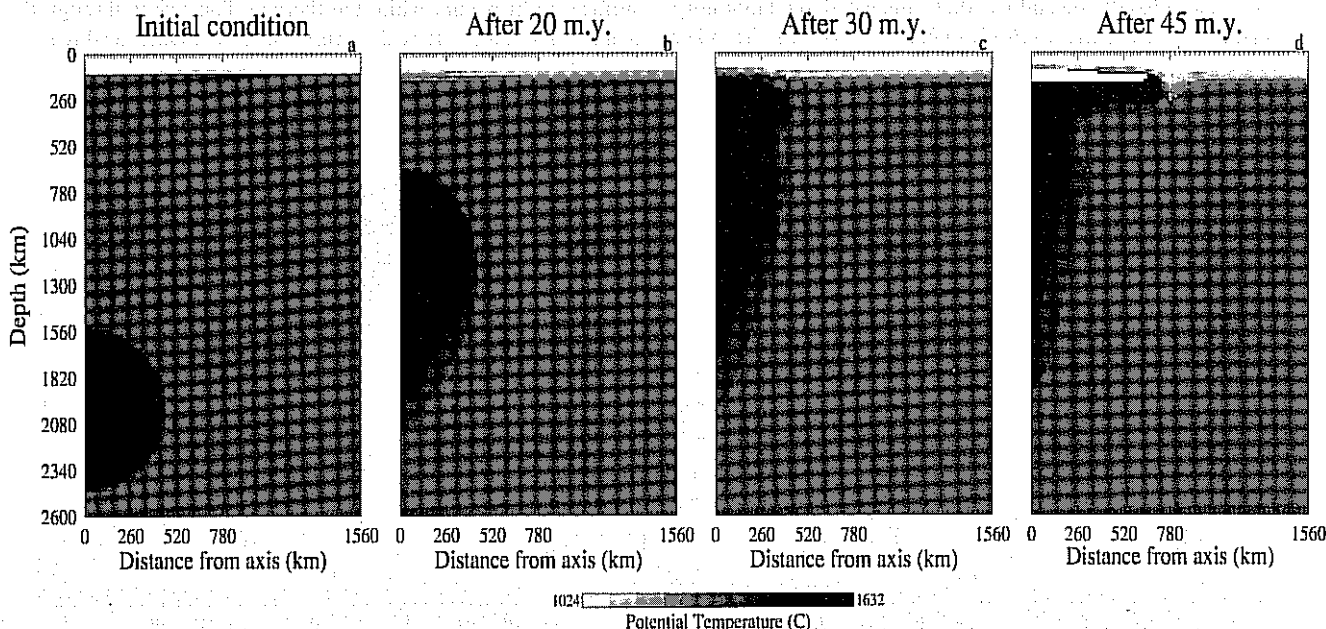

Figure 4. The evolution of the diapir with initial excess temperature $\Delta T_0 = 350°C$ and initial radius $R_0 = 400$ km. The mantle has a potential temperature $T_m = 1280°C$ and the mantle viscosity model is $\eta_{lm} = 10^{22}$ Pa s, $\eta_{um} = 10^{21}$ Pa s ($\gamma = 10$). (a) The initial condition. (b) After 20 m.y. (c) After 30 m.y. (d) After 45 m.y. The melting region is the white area beneath the lithosphere. To show the temperature structure of the diapir more clearly, the minimum potential temperature in the gray scale is 1024°C. This means the lithosphere (where $T < 1024°C$) is depicted in white.

Luther, 1975; *Campbell and Griffiths,* 1990] show that a newly formed thermal plume develops a large "head" and a "tail". The head forms since a large amount of buoyancy is needed before the plume is able to displace the overlying colder fluid and rise. The "tail" of thermal plumes is maintained by continued buoyancy flux from the bottom boundary. This tail is a somewhat arbitrary feature of the fluid dynamical experiments, since a constant buoyancy flux is imposed. Natural boundary layer instabilities arising in free convection may or may not be continuously fed from the boundary layer, depending on the particular conditions.

In the mantle plume initiation model, flood basalts are generated by melting of the head of the plume [*Morgan,* 1981; *Richards et al.,* 1989; *Campbell and Griffiths,* 1990], and in this first phase the contribution of the material rising through the tail is of secondary importance. Given the uncertainties in the details of how thermal instabilities would form at the CMB, we simply consider a hot, spherical diapir placed initially at 2000 km depth, which is not connected to any boundary layer. By doing this we avoid numerical modeling difficulties in resolving the tail, especially for the very thin conduits that would result in cases with strongly temperature dependent viscosity. The buoyancy of the thermal diapir is proportional to the excess temperature with respect to the mantle and to the cube of its radius. We investigate a range of initial radii $300 \leq R_0 \leq 500$ km and initial excess temperatures $300 \leq \Delta T_0 \leq 400°C$. The initial excess temperature ΔT_0 i s expected to be higher than the excess temperature (ΔT) estimated from petrologic constraints. The excess temperature that best fits the Hawaii hotspot swell is 200-300°C [*Sleep,* 1990], in agreement with a plume temperature of ~1500°C for magma generation beneath Hawaii [*Wyllie,* 1988]. The range of initial radius values we model is consistent with values estimated from laboratory experiments [*Campbell and Griffiths,* 1990] scaled to mantle conditions.

Mantle Viscosity Structure

Laboratory experiments have investigated the rise of a plume in a uniform viscosity fluid, but numerical modeling can address the effect of more realistic viscosity structures. Geophysical studies indicate that mantle viscosity may increase from the upper to the lower mantle by 1 or 2 orders of magnitude [e.g., *Hager,* 1984; *Nakada and Lambeck,* 1990]. Viscosity may change discontinuously at depth where phase changes occur, and it might vary continuously with depth due to the effects of pressure on the rheology of mantle materials.

We consider several viscosity structures and some temperature dependent viscosity cases. (We do not attempt to model other thermodynamical effects of phase changes.) In this study the values of the lower mantle viscosity (η_{lm}) range from 3×10^{22} to 3×10^{21} Pa s, and for the upper mantle viscosity (η_{um}) values range from 3×10^{21} to 3×10^{19} Pa s. This covers a reasonable range of mantle viscosities, though more extreme values are possible. The uniform mantle viscosity model has $\eta = 10^{21}$ Pa s. Figure 3 shows the viscosity profiles for the "standard" model ($\eta_{lm} = 10^{22}$ Pa s) for viscosity contrasts of $\gamma = 10$ and $\gamma = 100$ ($\gamma = \eta_{lm} / \eta_{um}$). The change in viscosity between the lower and upper mantle is at 670 km depth. The stiff rheology of the lithosphere is modeled by an increase in uppermost mantle viscosity up to 10^{22} Pa s (see next section). For temperature dependent viscosity we adopt the following exponential dependence:

$$\eta(T) = \eta_0 \exp(-4.60T) \tag{15}$$

which gives two orders of magnitude viscosity contrast across the lithosphere.

Lithosphere

The lithosphere is modeled by imposing an initial temperature profile and a viscosity structure (note that we concentrate on oceanic lithosphere for the reasons stated in the introduction). The initial temperature profile is given by an error function conduction profile [*Parson and Sclater,* 1977] according to the initial age. We investigate initial ages 0 Ma, 20 Ma, and 100 Ma. For nontemperature dependent viscosity cases, the viscosity of the lithosphere is 10^{22} Pa s from the surface to 55 km depth (for 100 Ma old lithosphere), or to 41 km depth (for 20 Ma and 0 Ma lithosphere). The viscosity decreases smoothly below these depths to upper mantle viscosity values (Figure 3). For a given initial age the viscosity structure of the uppermost 80 km is kept constant, independent of the values of the upper mantle viscosity (except for cases with temperature dependent viscosity). We note that these lithospheric viscosities are rather modest, so that we are generally modeling "best case" scenarios for melting due to the rise of hot plume material into the lower lithosphere.
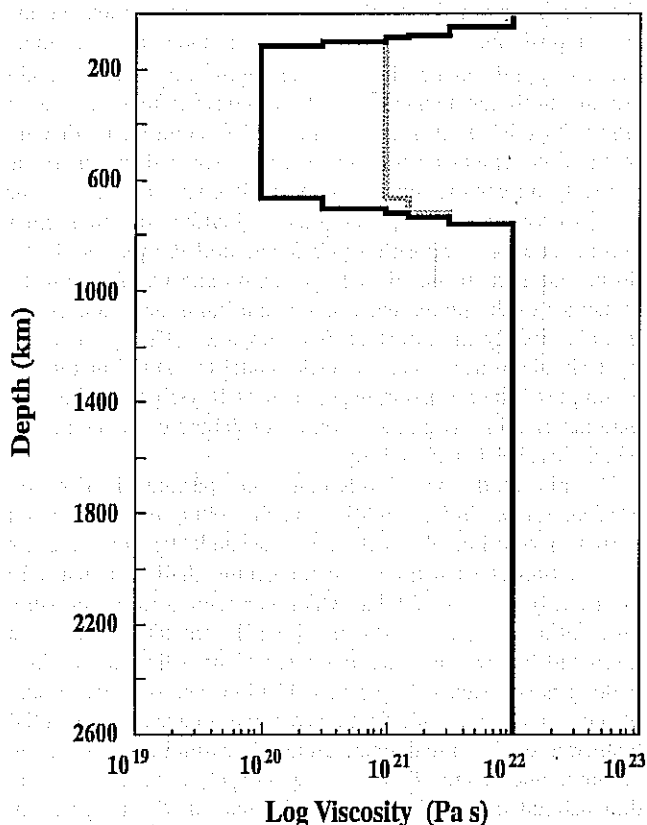
Viscosity Models

Figure 3. Mantle viscosity profiles for the two standard models: $\gamma = 10$ (thin line) and $\gamma = 100$ (thick line). $\gamma = \eta_{lm} / \eta_{um}$ is the ratio of lower mantle viscosity (η_{lm}) and upper mantle viscosity (η_{um}).

We also investigate the effects of lithospheric extension. If extension is allowed, we simply use a free radial slip boundary condition at the top surface nodes of the finite element grid. This allows extension to occur naturally since all internal nodes are unconstrained. For the majority of cases in which extension is not allowed, we impose zero radial velocity from the surface to 40 km depth for an initial age of 100 Ma, or to 28 km depth for 20 Ma lithosphere. It is important to note that the axisymmetry of our calculations requires that any horizontal extension be radial, so that we cannot generate more realistic models with unidirectional extension (rifting) of the lithosphere.

Results

The numerical model described above allows us to investigate the evolution of a thermal diapir as it rises in the mantle and impinges on oceanic lithosphere. We calculate the temporal and spatial variations of the surface uplift, the radial deviatoric (extensional) stress induced in the lithosphere, and the total melt volume. The model parameters vary about a "standard" case in which the thermal diapir has an initial excess potential temperature $\Delta T_0=350°C$, an initial radius $R_0=400$ km, the lower and upper mantle viscosities are $\eta_{lm}=10^{22}$ Pa s and $\eta_{um}=10^{21}$ Pa s, respectively ($\gamma=10$), the lithosphere is nonrifting and its initial age is 100 Ma. Figure 4 shows the time evolution of the thermal diapir for this standard model, starting from the initial condition (Figure 4a). After 20 m.y. (Figure 4b) the head of the diapir is at 670 km depth, while after 30 m.y. (Figure 4c) the plume head is at 180 km depth. Just prior to sublithospheric spreading the plume radius is ~350 km. Melting starts at 34 m.y. and increases as the plume head spreads beneath the lithosphere. The melting

region (for melt fraction $X>0\%$) is indicated in Figure 4d by the white area beneath the lithosphere. The maximum melt production occurs after 45 m.y. and the total melt volume produced is 3.7×10^6 km³. At this time the radius of the plume head is ~700 km and the radius of the melting region for melt fraction $X>5\%$ is ~580 km. Melting occurs at sublithospheric depths (100-150 km) since not enough time has elapsed for conductive heating the lithosphere above the solidus.

Figure 5 shows the time evolution of the initial diapir (Figure 5a) if the upper mantle viscosity is reduced to $\eta_{um}=10^{20}$ Pa s ($\gamma=100$) in the standard model. After 20 m.y. (Figure 5b) the head of the diapir is at 670 km depth. As it enters the upper mantle, a narrow conduit develops (with radius ~100 km) through which the hot material ascends at higher velocity, so that after only 24 m.y. (Figure 5c) the plume head is at ~180 km depth. The narrowing effect reduces the radius of the plume head impinging on the lithosphere to ~150 km. Melting starts after 24 m.y. and reaches a maximum after 33 m.y. (Figure 5d), the total melt volume produced is 2.6×10^6 km³. The radius of the plume head at this time is ~620 km, while the radius of the melting region, for melt fraction $X>5\%$, is ~360 km. The "narrowing" of the plume head is a consequence of the velocity increase of the buoyant fluid when it enters a lower-viscosity material [e.g., see *Richards et al.*, 1988]. The above figures illustrate that the viscosity structure of the mantle affects the dynamics of a rising plume and that 2 orders of magnitude viscosity contrast between the lower and upper mantle causes pronounced "necking". This ultimately influences the shape and size of the plume head and the radial extent of the melting zone.

For comparison, Figure 6 shows the evolution of the standard diapir (ΔT_0 and R_0 as above) rising in a uniform viscosity mantle ($\eta=10^{21}$ Pa s). No necking occurs, and the

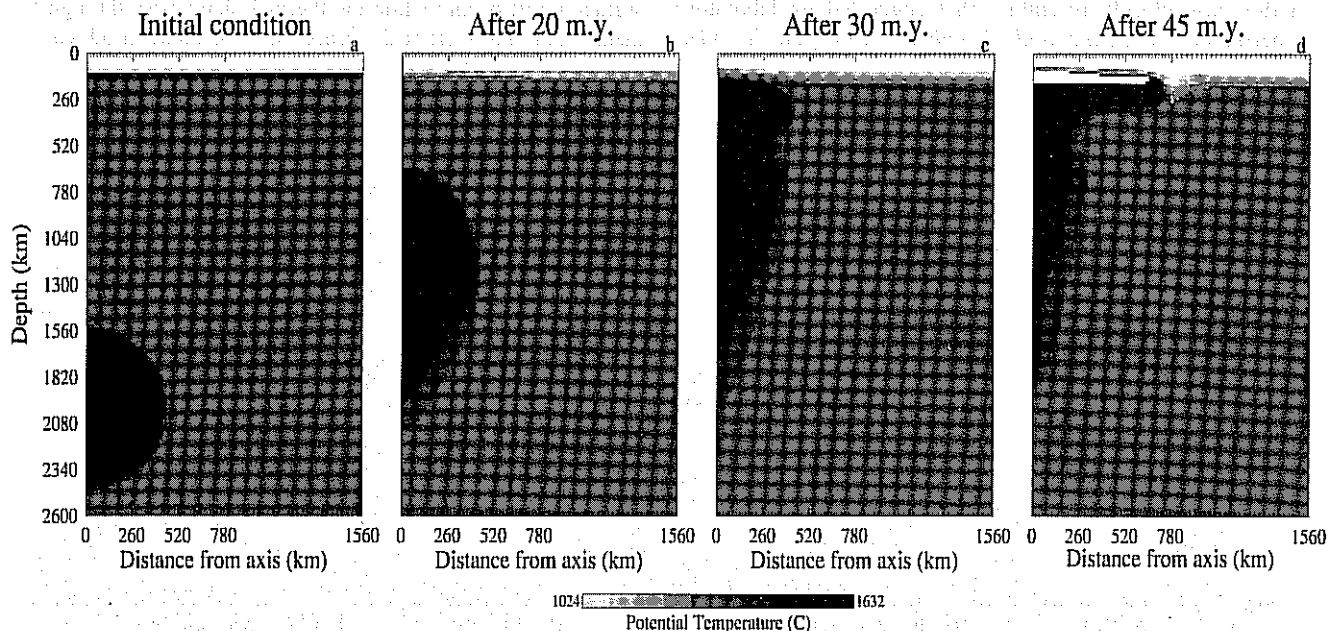**Figure 4.** The evolution of the diapir with initial excess temperature $\Delta T_0=350°C$ and initial radius $R_0=400$ km. The mantle has a potential temperature $T_m=1280°C$ and the mantle viscosity model is $\eta_{lm}=10^{22}$ Pa s, $\eta_{um}=10^{21}$ Pa s ($\gamma=10$). (a) The initial condition. (b) After 20 m.y. (c) After 30 m.y. (d) After 45 m.y. The melting region is the white area beneath the lithosphere. To show the temperature structure of the diapir more clearly, the minimum potential temperature in the gray scale is 1024°C. This means the lithosphere (where $T<1024°C$) is depicted in white.
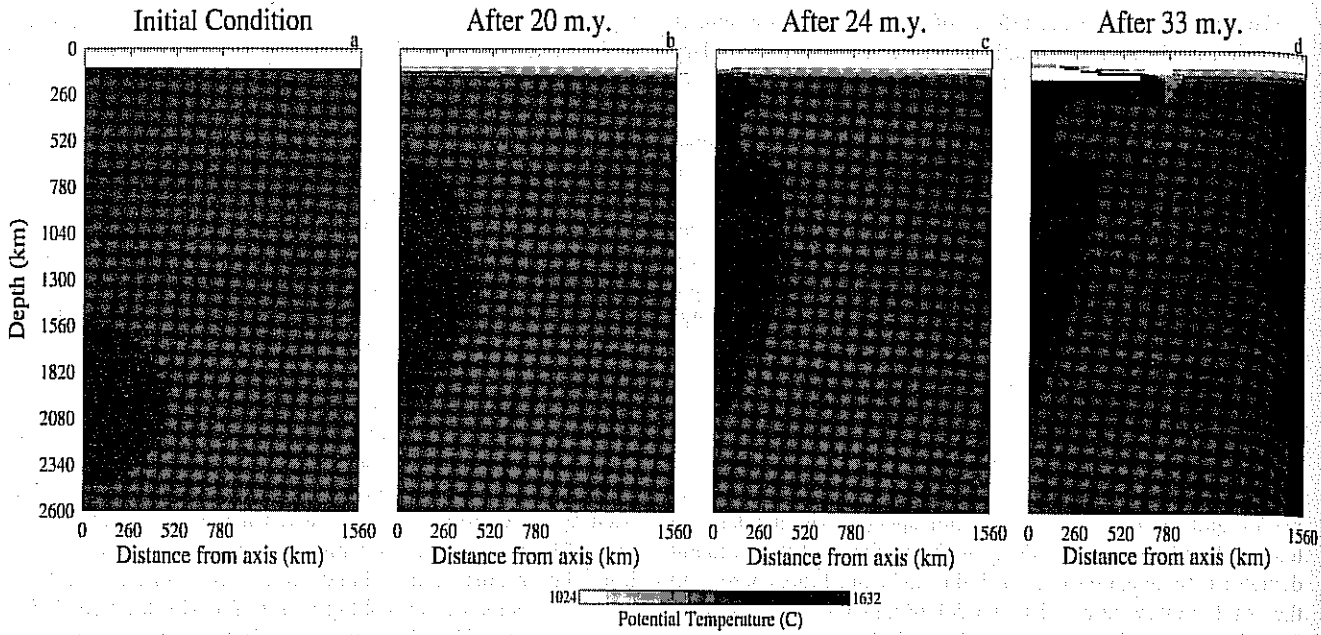
Figure 5. The evolution of the diapir with initial excess temperature $\Delta T_0=350°C$ and initial radius $R_0=400$ km. The mantle viscosity model is $\eta_{lm}=10^{22}$ Pa s, $\eta_{um}=10^{20}$ Pa s ($\gamma=100$). (a) The initial condition. (b) After 20 m.y. (c) After 24 m.y. Note the narrowing of the plume head ("necking" effect). (d) After 33 m.y. The melting region is the white area beneath the lithosphere.

diapir maintains a spherical shape as it ascends through the mantle (Figures 6a and 6b). When the plume head reaches the lithosphere, its radius is ~600 km (Figure 6c) and most of the buoyant material is contained in the head. Melting occurs at sublithospheric depths while the head spreads laterally to a radial distance of ~780 km (Figure 6d) and the total melt volume produced is 3.5×10^6 km³. The evolution of the diapir in this case closely resembles that suggested by laboratory experiments [*Griffiths and Campbell*, 1990]. On the other

hand, a uniform viscosity mantle is an unlikely model for the Earth, and we concentrate on cases with a viscosity contrast between upper and lower mantle.

Figures 7a and 7b show surface uplift (calculated on the axis of symmetry), melt volume, and radial deviatoric stress σ_{rr} (calculated on the axis of symmetry, at 80 km depth) as a function of time. For the standard case with $\gamma=10$ (Figure 7a), surface uplift occurs while the thermal diapir rises through the mantle, and the uplift peak occurs when the plume head reaches
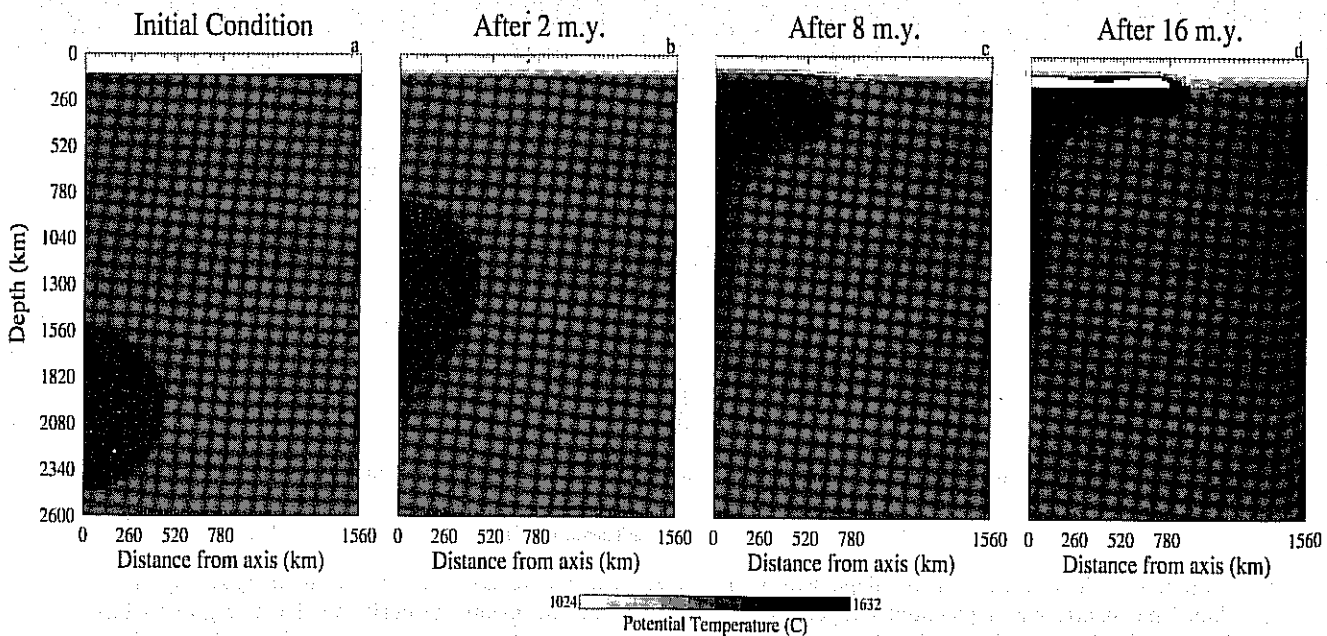

Figure 6. The evolution of the diapir with initial excess temperature $\Delta T_0=350°C$ and initial radius $R_0=400$ km. The mantle has a uniform viscosity $\eta=10^{21}$ Pa s. (a) The initial condition. (b) After 2 m.y. (c) After 8 m.y. (d) After 16 m.y. The melting region is the white area beneath the lithosphere.
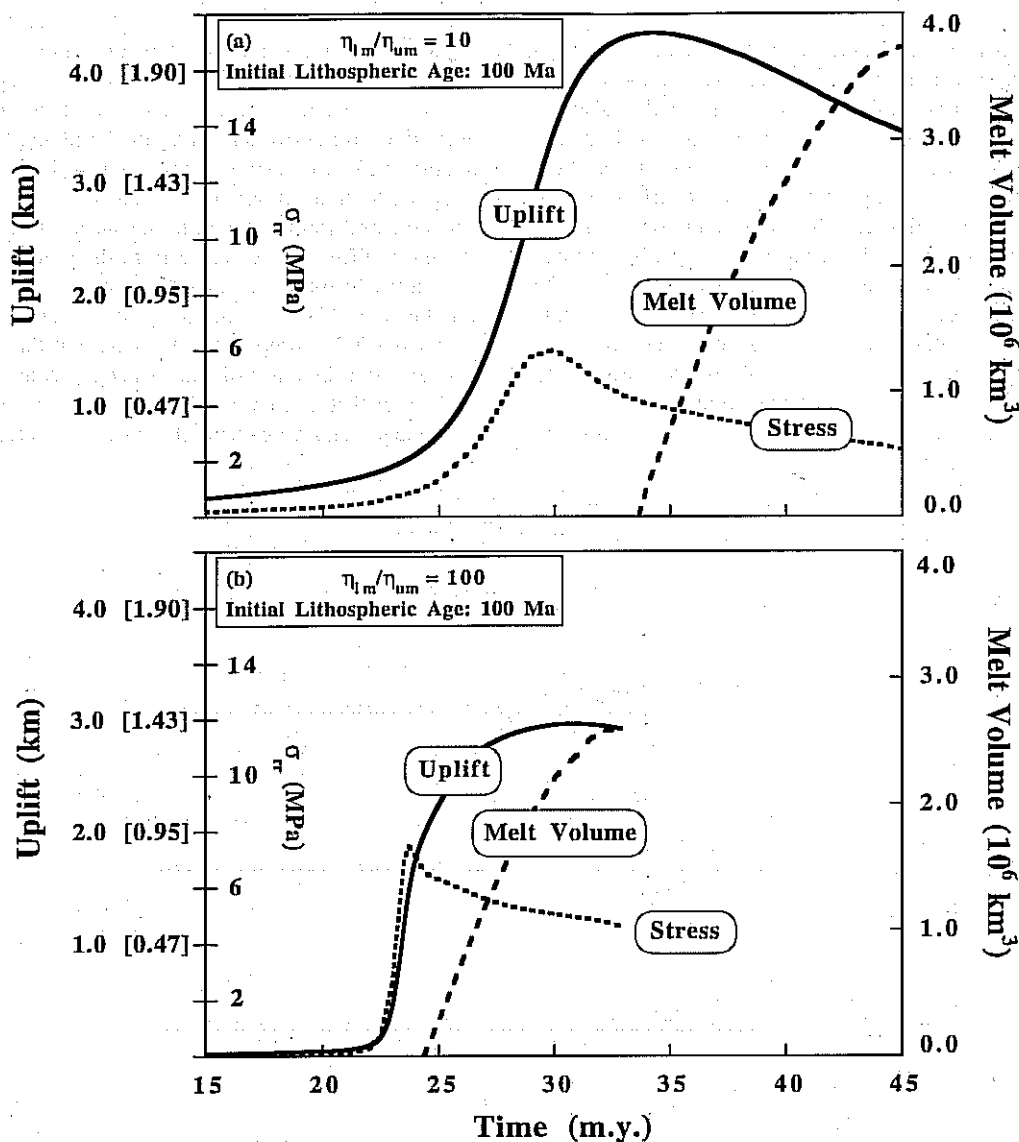
Figure 7. Uplift, radial deviatoric stress (σ_{rr}) and melt volume versus elapsed time. (a) For mantle viscosity contrast γ=10. (b) For γ=100. In both cases, ΔT_0=350°C and R_0=400 km. Note that the unbracketed and bracketed numbers on the uplift scale refer to maximum and minimum values, respectively. Maximum values are for the uplift from abyssal oceanic depths with a thermal expansion coefficient of 3×10^{-5} °C^{-1}. Minimum values are for subaerial uplift with a thermal expansion coefficient of 2×10^{-5} °C^{-1}.

the base of the lithosphere. Subsidence of the central area follows and accompanies the sublithospheric spreading of the head and melt production, as pointed out by *Griffiths and Campbell* [1991]. The peak of uplift precedes the peak of melt volume by ~10 m.y., so that subsidence of the central area occurs during the phase of maximum expected volcanism. The radial deviatoric (extensional) stress σ_{rr} is in phase with the uplift and the maximum extensional stress occurs when the plume head approaches the lithosphere. During the major melting phase, σ_{rr} gradually decreases. Figure 7b shows the time relation among uplift, melt volume, and radial deviatoric stress σ_{rr} for the standard case with γ=100. The surface uplift increases while the diapir rises through the mantle, while slow subsidence occurs during the sublithospheric spreading of the head. The peak of uplift precedes the peak of melt production by ~4 m.y. The deviatoric stress σ_{rr} reaches a maximum as the

plume head rises through the upper mantle, while during sublithospheric spreading σ_{rr} decreases. Note that the curves in Figures 7a and 7b terminate when the maximum melt volume is reached, and the extraction of melt (which we do not model) would certainly affect both the uplift and the melt volume.

Comparison of Figures 7a and 7b shows that for a higher-viscosity contrast (i.e., γ=100) both peaks in uplift and melt volume occur earlier in time, which is consistent with the fact that the head ascends more rapidly in the upper mantle. The maximum amount of uplift decreases and the total melt volume is reduced modestly, probably due to the narrowing of the plume head. Reducing the upper mantle viscosity serves mainly to compress the time scale for these events and, to a lesser degree, the horizontal length scale of the plume activity. We also see that, independent of the viscosity

structure, the peak of uplift precedes the peak of melt production, so that the model predicts a regular time sequence of uplift, thermal subsidence, and volcanic activity.

Figure 8 shows surface uplift as a function of radial distance from the axis, at different time steps and for the standard case ($\gamma=10$). Note that the constraints of conservation of mass and incompressibility cause negative values of uplift at the extreme right of the cylinder. While the diapir rises through the lower and upper mantle, the surface is affected by a broad, low-amplitude swell (see curves at elapsed time 22 and 26 m.y.). The central uplift increases considerably as the plume head approaches the lithosphere (26 to 34 m.y.) and affects an area ~400 km in radius. After 34 m.y., subsidence starts on the axis, but at greater distances, uplift may continue for several million years, as the plume head spreads beneath the

lithosphere. Consequently, the onset of thermal subsidence does not occur simultaneously over the whole swell. Figure 8 also shows the radial extent of the melting region for melt fractions $X>5\%$ and $X>10\%$. The extent of the melting region reflects the progressive spreading of the plume head, and it is probably safe to assume that areas where $X \geq 5\%$ will correspond to areas of surface volcanism.

The temporal relation between the surface uplift and melting will clearly differ with distance from the plume axis. Figure 9 shows uplift histories at radial distances 0, 250, and 500 km from the axis. The maximum uplift at 250 km distance is reduced to ~80%, compared to the axis, but the timing for the uplift peak and the onset of subsidence are comparable, so that we can infer that a fairly regular time sequence of uplift, onset of subsidence and volcanism should be expected in a central
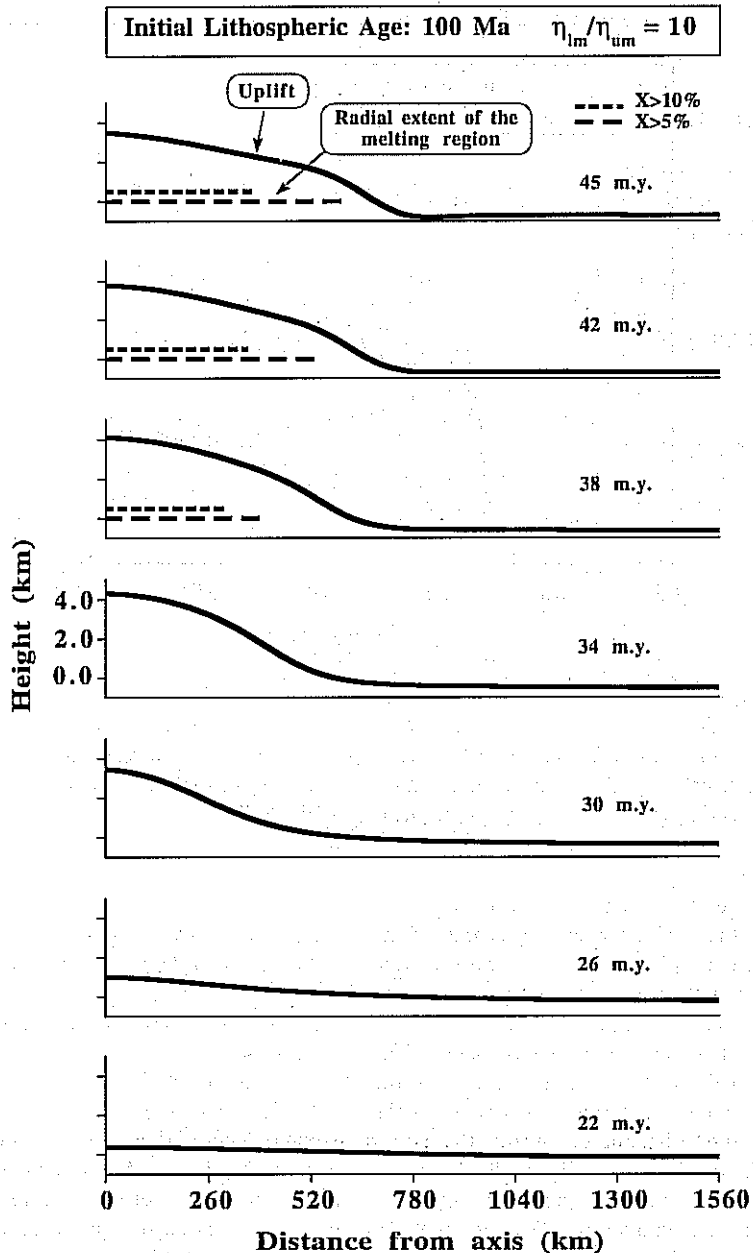

Figure 8. Surface uplift versus axial distance at different elapsed times. The radial extent of the melting region for melt fraction $X>5\%$ (long dashed line) and $X>10\%$ (short dashed line) is indicated. The initial diapir has $\Delta T_0=350°C$ and $R_0=400$ km and the mantle viscosity contrast is $\gamma=10$. The vertical exaggeration is 50:1.
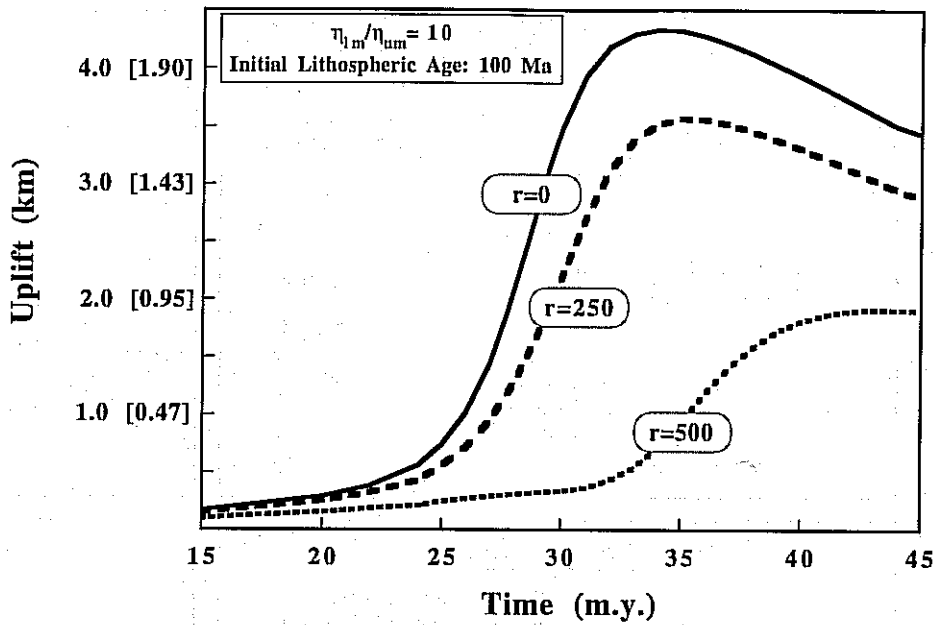
Figure 9. Uplift versus elapsed time calculated at radial distance from the axis $r=0$, 250, and 500 km. The initial diapir has $\Delta T_0=350°C$ and $R_0=400$ km, and the mantle viscosity contrast is $\gamma=10$. Note that the unbracketed and bracketed numbers on the uplift scale refer to maximum and minimum values, respectively. Maximum values are for the uplift from abyssal oceanic depths and with a thermal expansion coefficient of 3×10^{-5} °C^{-1}. Minimum values are for subaerial uplift with a thermal expansion coefficient of 2×10^{-5} °C^{-1}.

area ~300-350 km in radius. At a distance of 500 km the uplift occurs only in the latest stages, after the plume head has spread beneath the lithosphere, and thus the volcanic activity may be synchronous with the uplift phase.

Figure 10 compares the uplift and melting history for three mantle viscosity models. The lower mantle viscosity is $\eta_{lm}=3\times10^{21}$ Pa s (for model A), $\eta_{lm}=10^{22}$ Pa s (for model B), and $\eta_{lm}=3\times10^{22}$ Pa s (for model C), the corresponding upper
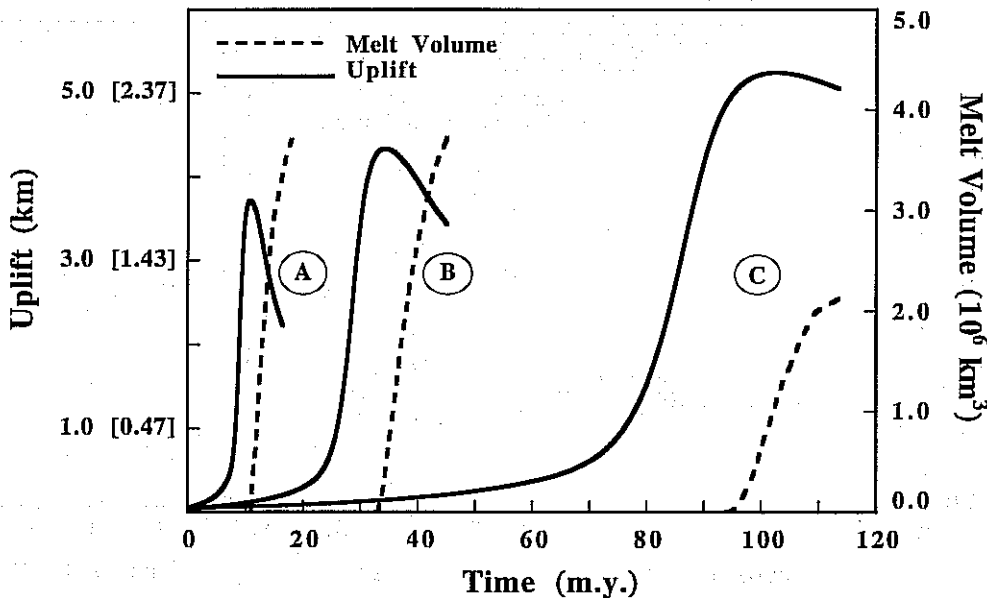

Figure 10. Uplift (solid line) and melt volume (dashed line) history for viscosity model A, $\eta_{lm}=3\times10^{21}$ Pa s, $\eta_{um}=3\times10^{20}$ Pa s; viscosity model B, $\eta_{lm}=10^{22}$ Pa s, $\eta_{um}=10^{21}$ Pa s; viscosity model C, $\eta_{lm}=3\times10^{22}$ Pa s, $\eta_{um}=3\times10^{21}$ Pa s. For all models the initial diapir has $\Delta T_0=350°C$, $R_0=400$ km and the initial age of the lithosphere is 100 Ma. Note that the unbracketed and bracketed numbers on the uplift scale refer to maximum and minimum values, respectively. Maximum values are for the uplift from abyssal oceanic depths and with a thermal expansion coefficient of 3×10^{-5} °C^{-1}. Minimum values are for subaerial uplift with a thermal expansion coefficient of 2×10^{-5} °C^{-1}.
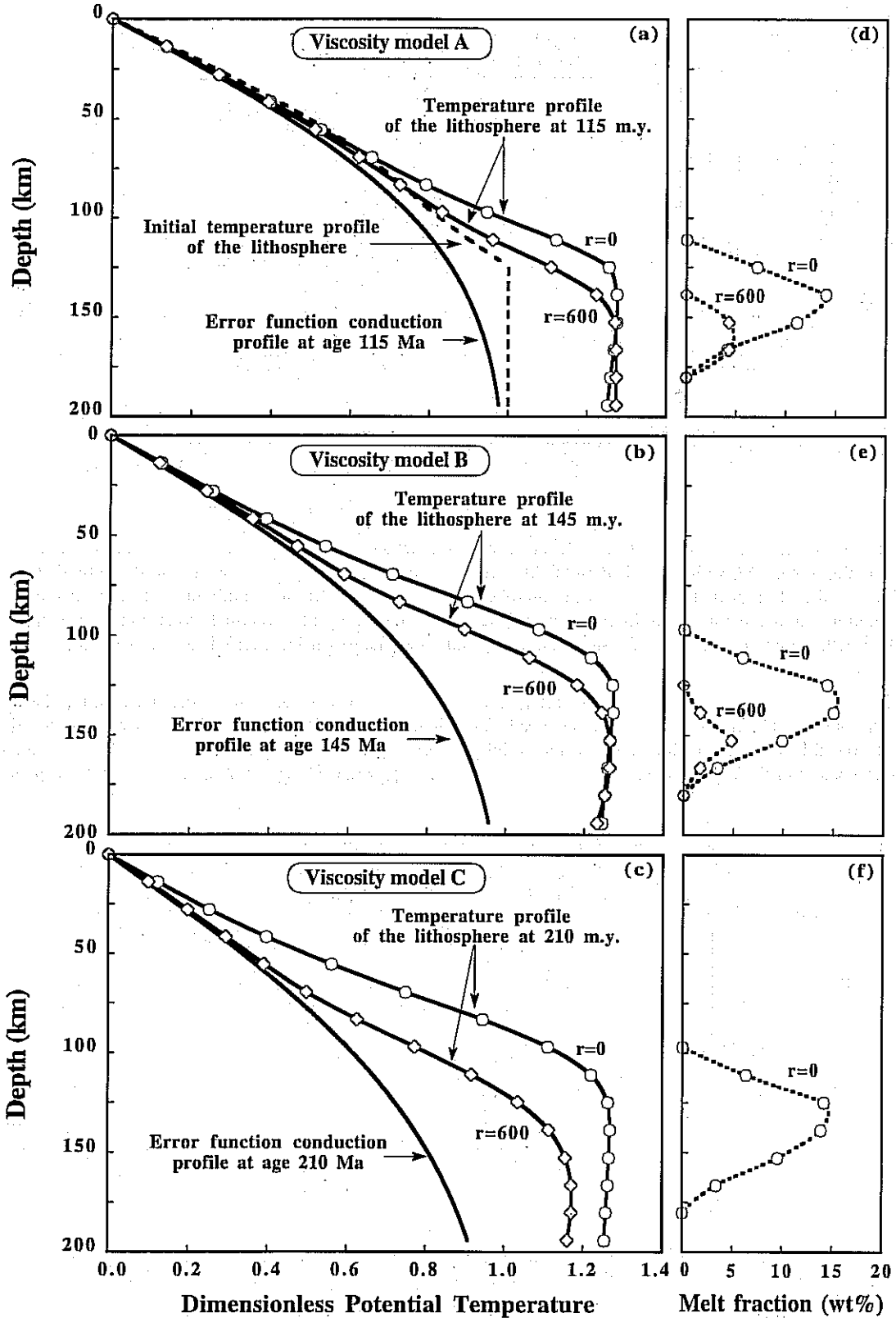
Figure 11. (left) Dimensionless potential temperature versus depth. The solid line is the error function conduction profile calculated at the time of maximum melt production. The temperature profile of the lithosphere is indicated at radial distance $r=0$ km from the axis (solid line with circles) and $r=600$ km (solid line with diamonds). Note that each symbol corresponds to a node in the finite element grid. The dashed line in Figure 11a is the initial temperature profile for a 100 Ma old lithosphere imposed as initial condition in all models. (a) For viscosity model A, $\eta_{lm}=3\times10^{21}$ Pa s, $\eta_{um}=3\times10^{20}$ Pa s. (b) For viscosity model B, $\eta_{lm}=10^{22}$ Pa s, $\eta_{um}=10^{21}$ Pa s. (c) For viscosity model C, $\eta_{lm}=3\times10^{22}$ Pa s, $\eta_{um}=3\times10^{21}$ Pa s. (right) Distribution of the melt fraction with depth at radial distance $r=0$ and $r=600$ km. (d) For viscosity model A. (e) For viscosity model B. (f) For viscosity model C. In all the models the initial diapir has $\Delta T_0=350°C$, $R_0=400$ km.

mantle viscosities satisfy $\gamma=10$. For all models the initial diapir has $\Delta T_0=350°C$ and $R_0=400$ km, the initial age of the lithosphere is 100 Ma and extension is not allowed. The viscosity of the mantle governs the ascent rate of the diapir. For the two extreme viscosity models considered (i.e., A and C), the diapir rise times differ by an order of magnitude (10 m.y. versus 100 m.y.). Higher values of the mantle viscosity increase the lag time between peak uplift and magmatism and increase the maximum uplift. The total melt volume is instead reduced (~30%), since the progressive aging and cooling of the lithosphere tend to inhibit melting. Figures 11a, 11b, and 11c show the temperature profile of the lithosphere for the viscosity models A, B, and C, respectively. The profiles are given at radial distances $r=0$ and $r=600$ km from the axis of symmetry and are calculated at the time of maximum melt production. The temperature difference between these profiles and the theoretical error function profile, calculated at the same age, indicates the amount of "thermal rejuvenation" of the lithosphere. For viscosity model A (Figure 11a) the temperatures are higher than the expected (~20-30%) only from 60 km depth to the base of the lithosphere (~100 km depth), thus suggesting that the lithosphere is not significantly heated by conduction. The profile at $r=600$ km is similar to the one on the axis, since the low viscosity of the

sublithospheric mantle facilitates the radial spreading of the plume head. By contrast for viscosity model C (Figure 11c) the temperatures from 20 to 100 km depth, can be 20 to 70% higher than the expected values, at radial distances $r=0$ km. In this case the plume head tends to pond beneath the lithosphere since its radial spreading is inhibited by the high viscosity of the upper mantle. This also explains the modest increase in temperature at distance $r=600$ km, compared to the profile at $r=0$ km. However, we note that melting always occurs at sublithospheric depths (i.e., deeper than ~100 km), as indicated in Figures 11d, 11e, and 11f, where we plot the melt fraction versus depth for the viscosity models A, B, and C, respectively. We also find that over the whole range of mantle viscosity structures investigated the variation in melt volume is very modest (from 2 to 4×10^6 km³), probably because thermal rejuvenation counterbalances the progressive aging of the lithosphere.

For a few models we have considered the effect of temperature dependent viscosity. As discussed previously, we use the law $\eta(T)=\eta_0 \exp(-4.60T)$. The viscosity contrast across the lithosphere is 2 orders of magnitude, while the diapir viscosity is 3.5 times less than that of the surrounding material (for an initial excess temperature of 350°C). Figure 12 shows the uplift and melting history for a temperature
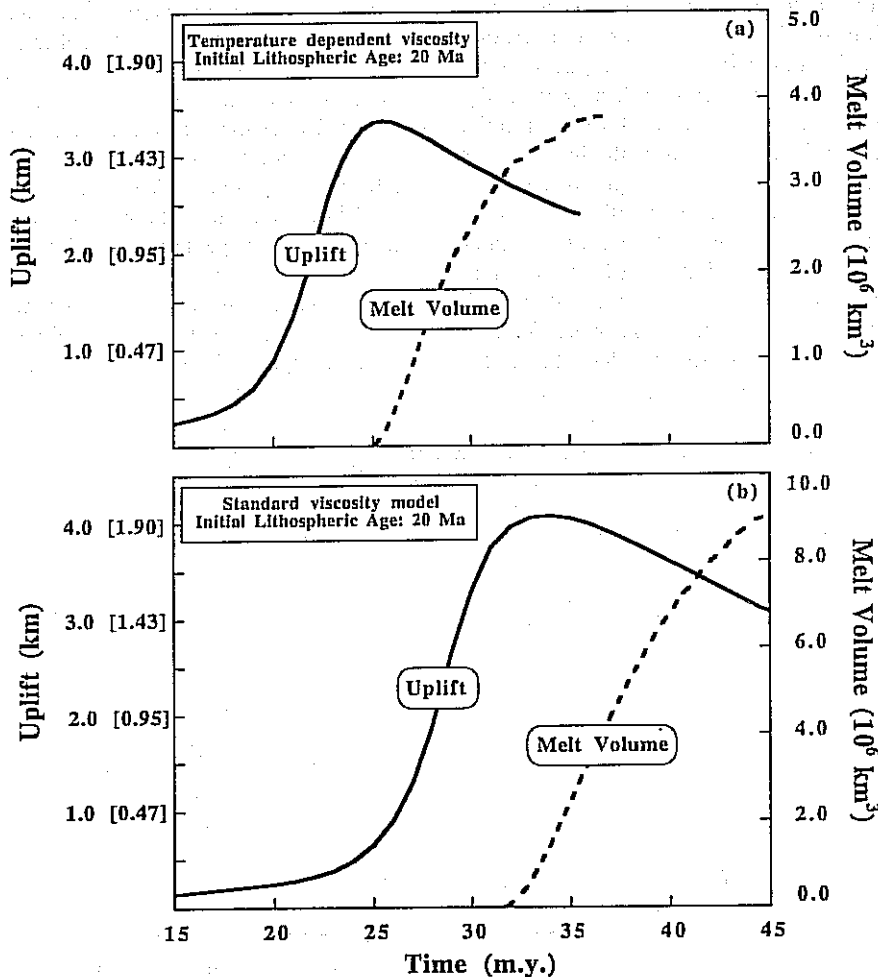

Figure 12. Uplift and melt volume versus elapsed time. (a) For the temperature dependent viscosity case. (b) For the standard viscosity model. In both cases, $\Delta T_0=350°C$ and $R_0=400$ km. Note that the unbracketed and bracketed numbers on the uplift scale refer to maximum and minimum values, respectively. Maximum values are for the uplift from abyssal oceanic depths and with a thermal expansion coefficient of 3×10^{-5} °C^{-1}. Minimum values are for subaerial uplift with a thermal expansion coefficient of 2×10^{-5} °C^{-1}.

dependent viscosity case (Figure 12a) and for the standard viscosity model (Figure 12b). In both cases the initial lithospheric age is 20 Ma and lithospheric extension above 30 km depth is prevented by setting the radial velocity to zero. For the case with temperature dependent viscosity, both uplift and melt production peak earlier in time, since the low-viscosity thermal diapir rises more rapidly in the mantle. Because of the stiffer behavior of the lithosphere, melting occurs at greater depth, and thus the total melt volume produced is reduced to $\sim 4 \times 10^6$ km^3 (for the standard model the melt volume is $\sim 9 \times 10^6$ km^3). This suggests that the standard lithospheric structure is fairly weak and thus represents a "best case" scenario for the rise of the plume head to shallower depths. We have found that temperature dependent viscosity has only modest (and quite predictable) effects upon the sublithospheric fluid dynamics of our model. Little heat is conducted into the upper lithosphere and crust, so that, within the model we have specified, little softening of the lithosphere occurs prior to melting. Of course, heat transfer by mass transfer (melt migration) may be important, but we have not attempted to model that effect. Still, we are confident that the most important factor is whether or not the uppermost lithosphere extends freely, and a more sophisticated treatment is needed to address this issue fully.

We next investigate the effect of the initial diapir size and the excess temperature. Figure 13 shows the maximum melt volume as a function of the initial excess temperature ($300 \leq \Delta T_0 \leq 400°$C) and initial radius ($300 \leq R_0 \leq 500$ km), for a model with $\eta_{lm} = 10^{22}$ Pa s and $\eta_{um} = 10^{21}$ Pa s ($\gamma = 10$) and a nonrifting lithosphere with initial age of 20 Ma. For an initial excess temperature of 300°C, independent of the initial radius of the diapir, the melt volume generated is equal or less than 10^6 km^3. Given such a low value, compared with the estimates for large flood basalts and oceanic plateaus, we consider $\Delta T_0 = 300°$C as a lower bound for the initial excess temperature of the diapir (for nonrifting lithosphere). The melt volume strongly depends on ΔT_0, since both the melt fraction produced at a given depth and the pressure at which the solidus

is intersected are functions of the excess temperature of the diapir. The melt volume also increases with increasing R_0; this result is fairly intuitive, but we also find that the melt volumes produced for $R_0 = 500$ km at $\Delta T_0 \sim 300$-330°C are relatively low. We find that the curvature of the upper part of the plume head first impinging on the lithosphere decreases with increasing R_0. A large flat head does not seem to efficiently remove, by lateral flow, the thin layer of material trapped between the stiff lithosphere and the plume head. The behavior of this "squeeze layer" [*Griffiths and Campbell*, 1991] and its ability to drain horizontally affect the depth to which the plume head ascends and melts and may explain the relative low melt volumes obtained for $R_0 = 500$ km at $\Delta T_0 \sim 300$-330°C. For $\Delta T_0 > 330°$C this effect becomes less relevant, probably because the conductive heat transport between the plume head and the lithosphere is more efficient due to the higher-temperature gradients. (We checked that this effect is not a function of the width of the finite element domain by increasing the radius of the domain to 2300 km while maintaining the same element size.)

The next set of models addresses the effect of the initial lithospheric age on the total melt volume. Figure 14 shows the melt volume as a function of the initial excess temperature ($300 \leq \Delta T_0 \leq 400°$C) for initial lithospheric ages of 20 and 100 Ma. In these models, lithospheric extension is prevented, and we use $R_0 = 400$ km, $\eta_{lm} = 10^{22}$ Pa s and $\eta_{um} = 10^{21}$ Pa s. For the case of a young oceanic lithosphere, the total melt volume produced ranges between 1 and 17×10^6 km^3, while for an old lithosphere the melt volumes are reduced approximately by a factor of 2 over the temperature range investigated. We also show the effect of varying the entropy of fusion from the usually adopted value of 250 J kg^{-1} °K^{-1} (solid line), to 400 J kg^{-1} °K^{-1} (dashed line). The melt volume is reduced by $\sim 30\%$ over the whole temperature range investigated. *McKenzie and Bickle* [1988] suggest that if $\Delta S = 400$ J kg^{-1} °K^{-1} is used in the melting model, then the required potential temperature of the mantle (T_m) is 1300°C, rather than 1280°C. The solid symbols in Figure 14 are for two test cases, with $\Delta S = 400$ J kg^{-}
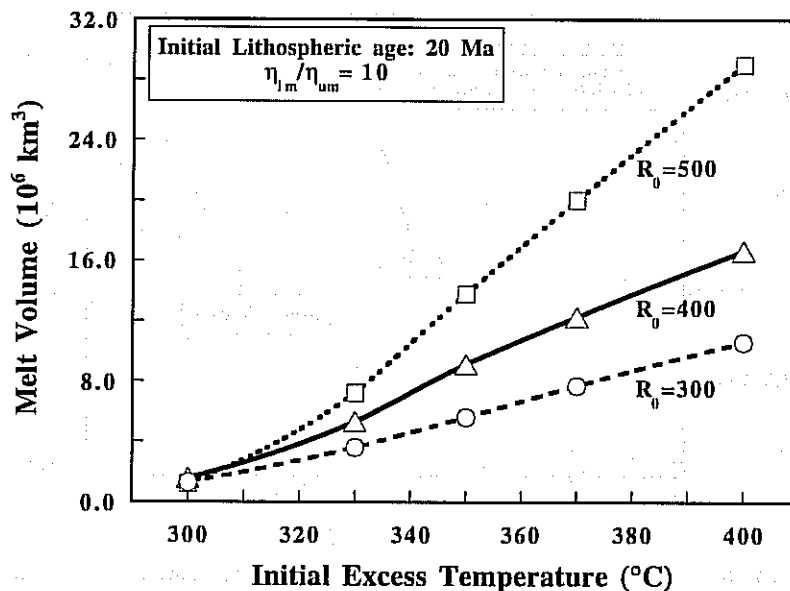

Figure 13. Total melt volume versus initial excess temperature for initial diapir radius $R_0 = 300$ km (long dashed line), $R_0 = 400$ km (solid line), $R_0 = 500$ km (short dashed line).
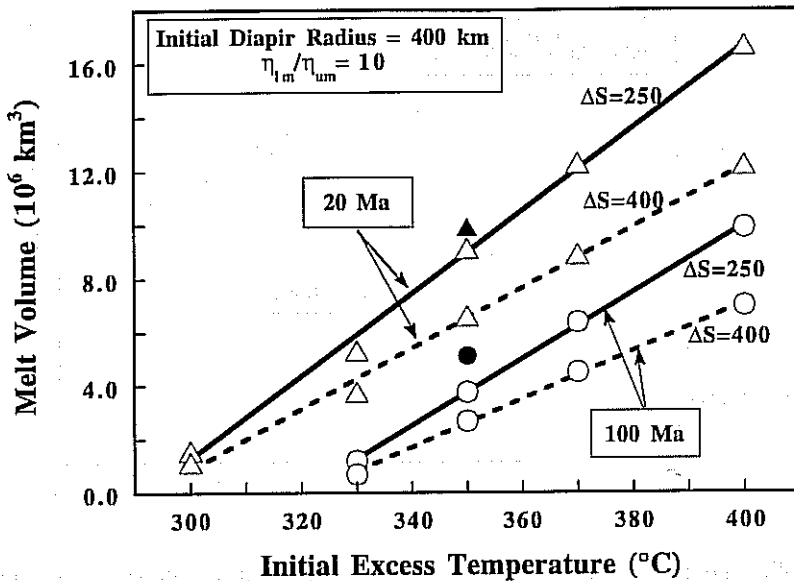
Figure 14. Total melt volume versus the initial excess temperature for initial lithospheric age of 100 Ma (lines with open circles) and 20 Ma (lines with open triangles). The entropy of fusion used in the melting model is $\Delta S=250$ J kg^{-1} °K^{-1} (solid lines) and $\Delta S=400$ J kg^{-1} °K^{-1} (dashed lines). In all cases the potential temperature of the mantle is $T_m=1280$°C. The two solid symbols are calculated using $\Delta S=400$ J kg^{-1} °K^{-1} and $T_m=1300$°C.

[1] °K^{-1} and $T_m=1300$°C, and indeed the melt volumes are comparable with the ones of the standard model.

The case of initially zero age lithosphere is treated separately, since we also change the top boundary condition to radial free slip, thus allowing the lithosphere to extend. This has a major effect on the melt volumes, which increase by an order of magnitude (i.e., ~50x10^6 km^3, for $\Delta T_0=350$°C and $R_0=400$ km) as melting occurs at shallow depths (20-100 km) with melt fractions as high as ~30%. Table 2 shows the melt volumes, the depth of the melting zone, and the mean MgO concentration for initial lithospheric ages of 0, 20, and 100 Ma, if extension is allowed. Melt volumes generated with $\Delta T_0=350$°C are of order 40-50x10^6 km^3, independent of the initial age of the lithosphere and the viscosity model. (The results are given for the standard model with $\eta_{lm}=10^{22}$ Pa s and $\eta_{um}=10^{21}$ Pa s, and for a model with temperature dependent viscosity.) For a rifting case, even an initial excess temperature as low as $\Delta T_0=250$°C can produce melt volumes of

~28x10^6 km^3, while if extension is prevented the melt volume produced is negligibly small (0.03x10^6 km^3). However, the axisymmetric geometry is not entirely appropriate to modeling unidirectional extension (rifting) over a mantle plume, and thus the calculated melt volumes should be considered as upper bounds, approximating the scenario of a plume head impinging on a ridge-ridge-ridge triple junction.

Figure 15 illustrates the uplift and melt volume calculated when lithospheric extension is allowed. The uplift generated for rifting models appears to be very large, exceeding 5 km in some cases. However, this is somewhat an artifact of the reference level chosen. Calculated uplift is the total amplitude of surface deformation from the axis to the outside edge of our model domain, so "extra" uplift arises from lithospheric thinning above the plume and lithosphere sinking at the outer edge. In other words, the uplift is effectively referenced to abyssal depths (typically 5-6 km) as opposed to normal ridge depth, so that even a model uplift of the ocean floor of 5 km

Table 2. Models with Lithospheric Extension Allowed

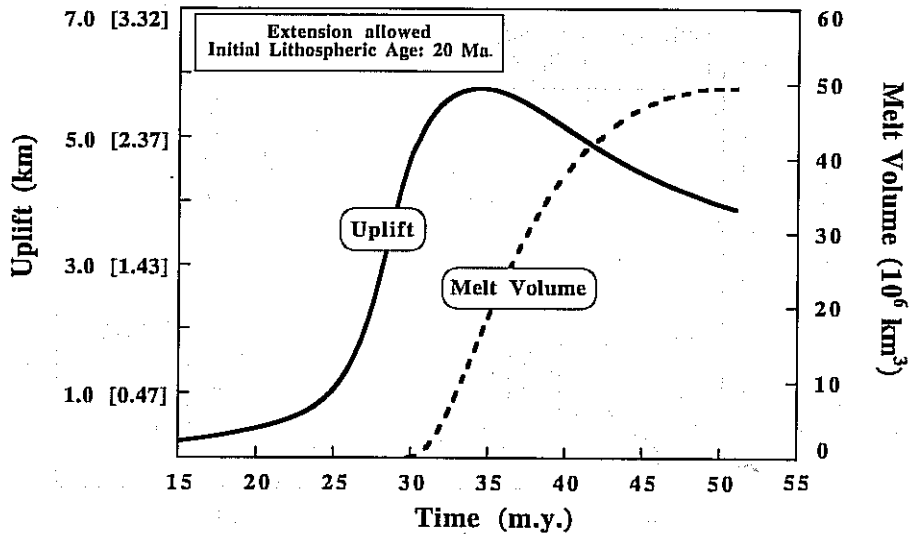| ΔT_0,	Initial Age,	Extension Allowed	Viscosity Model	Melt Volume,	Depth of Melting,	Maximum Melt Fraction,	Mean MgO,
°C	Ma			x10^6 km^3	km	wt %	wt %
250	20	no	standard	0.03	–	–	–
250	20	yes	standard	28	20-100	~30	15.5
350	20	no	standard	9	75-150	~22	18
350	20	yes	standard	49	20-130	~34	18
350	20	yes	η(T)	41	20-100	~28	18
350	100	no	standard	4	100-150	~14	17.5
350	100	yes	standard	45	20-130	~30	18
350	100	yes	η(T)	39	20-110	~30	17.5
350	0	yes	standard	50	20-130	~35	18.5

Figure 15. Uplift and melt volume versus elapsed time if extension allowed. The initial age of the lithosphere is 20 Ma, the diapir has $\Delta T_0 = 350°C$ and $R_0 = 400$ km, the mantle viscosity model is $\eta_{lm} = 10^{22}$ Pa s, $\eta_{um} = 10^{21}$ Pa s. Note that the unbracketed and bracketed numbers on the uplift scale refer to maximum and minimum values, respectively. Maximum values are for the uplift from abyssal oceanic depths and with a thermal expansion coefficient of 3×10^{-5} °C^{-1}. Minimum values are for subaerial uplift with a thermal expansion coefficient of 2×10^{-5} °C^{-1}.

may not represent uplift above sea level. Thus the "dynamic" component of uplift due to the plume does not exceed that obtained in the nonrifting case.

The batch melting model of *McKenzie and Bickle* [1988] allows us to estimate the average melt compositions in each model. Though we calculate the concentrations of all the major oxides in the melt, we consider MgO concentration to be the most indicative concerning the nature of the primary magma. The mean MgO concentration is obtained as a weighted average over the whole melting region. Figure 16 shows the mean MgO concentration, evaluated at the time of maximum melt production, as a function of the initial excess temperature of the diapir. The results are given for initial lithospheric ages of 100 and 20 Ma, when the initial radius of the diapir is 400 km. The mean MgO concentration ranges between 16 and 19 wt %, the higher values being obtained for higher initial excess temperatures and for younger lithospheric ages. These very high MgO concentrations result from the great depth and the large degree of melting in all cases. Similar values for MgO are found also for the rifting models (see Table 2).

Discussion

We have investigated the rise of a thermal diapir in the mantle and its interaction with the lithosphere prior to and during melting, using a numerical model that combines mantle flow dynamics with a batch melting model. Our numerical approach allows us to develop more fully some predictions of the mantle plume initiation model and to analyze quantitatively their dependence on the model parameters. Hopefully, this will form a stronger basis for comparison with field and analytical data. In this study we did not attempt to satisfy the specific characteristics of any single flood basalt or oceanic plateau. Instead, we wanted to explore the conditions under which it is possible to obtain melt volumes and compositions, melt production rates, degrees of uplift,

etc., which are comparable to those observed or inferred from field studies.

One issue we set out to address was the effect of mantle viscosity structure on observable aspects of mantle plumes. We have investigated viscosity contrasts ($\gamma = \eta_{lm} / \eta_{um}$) from lower to upper mantle of 1 ($\gamma = 10$) and 2 ($\gamma = 100$) orders of magnitude. A high-viscosity contrast induces a narrowing of the plume head as it enters the upper mantle. This "necking" occurs because the rise velocity of the plume head increases as the viscosity of the surrounding medium is decreased. The necking of the plume head causes a reduction of both the radius of the plume head first impinging on the lithosphere and the radial extent of the melting region. Moreover, for a model with $\gamma = 100$, a large volume of the diapir remains in the lower mantle for 10-20 m.y., favoring the entrainment of lower mantle material, while upper mantle material seems to be less easily entrained given the limited surface extent of the narrow conduit. Thus the effect of thermal entrainment in this case would differ in detail from the one suggested by *Griffiths and Campbell* [1990] for a uniform viscosity mantle.

We have also attempted to constrain the initial excess temperature of rising plume heads, treating the case of nonrifting lithosphere as the most stringent test. We find that for the *McKenzie and Bickle* [1988] batch melting model employed, rising plume heads must be at least 300°C hotter than normal mantle in order to obtain melt volumes of ~1×10⁶ km³ for models without lithospheric extension. This lower bound on initial excess temperatures is ~100°C higher than the one estimated from laboratory experiments [*Griffiths and Campbell,* 1990], which does not account for the presence of the lithosphere. Furthermore, we find that a diapir with an initial radius of 400 km needs to have an initial excess temperature of 350°C in order to generate melt volumes of ~3-9×10⁶ km³ if the lithosphere is older than 20 Ma and if extension is prevented. (Note that the results for initial lithospheric age of 100 Ma might be considered as "upper
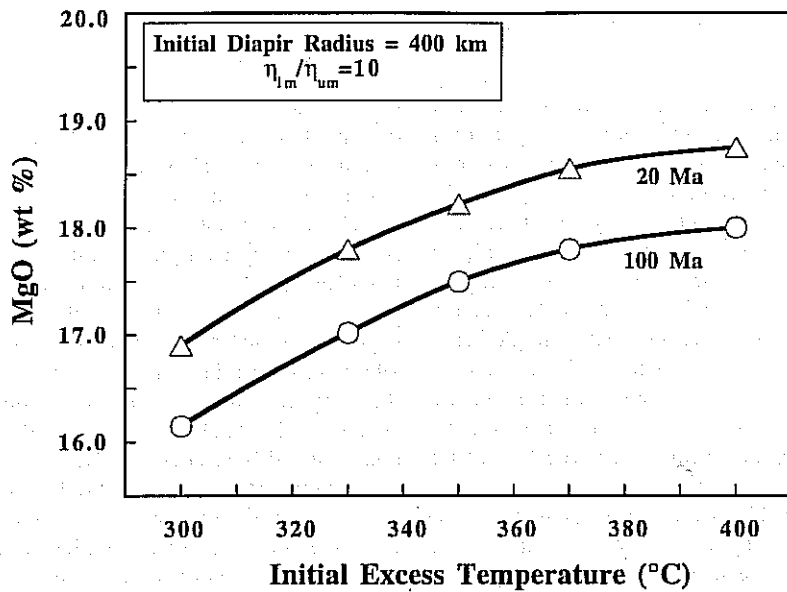
Figure 16. Mean MgO concentration of the melt versus the initial excess temperature of the diapir for models with initial lithospheric age of 100 and 20 Ma.

bounds" for an ancient cratonic continental lithosphere, whose thickness may, in fact, be considerably greater than that of old oceanic lithosphere.) At the onset of melting the potential temperature of the plume head is ~1600°C, although it decreases somewhat in time due to the latent heat of melting.

The melt volume generated from these hot plume heads greatly depends on the ability of the plume to ascend to shallower depths, and decompression melting is an efficient way to produce large melt volumes. We found that for the models where surface extension is not allowed, the depth range of partial melting is mostly (~90%) sublithospheric, since there is not enough time to heat the lithosphere by conduction above the solidus before the plume head has spread and cooled considerably. This conclusion is in agreement with the work of *Arndt and Christensen* [1992] on the role of lithospheric mantle in continental flood volcanism, which shows that the bulk of primary magmas is produced by melting of a plume at sublithospheric depths (>100 km). The geochemical signature of the volcanic products can constrain the depth of melting, and indeed, there is growing evidence that some of the earliest magmas in flood basalts represent low degrees of partial melt formed in the garnet stability field. For the Siberian Traps this is indicated by the depletion of heavy rare earth elements, combined with high incompatible element contents in the initial lava suites [*Wooden et al.,* 1993]. Similarly, for the Kerguelen Plateau, trace element and isotopic characteristics indicate that the onset of melting has to be placed in the garnet stability field [*Salters et al.,* 1992]. Also the depth of melting derived from rare earth element inversions over plumes [*White et al.,* 1992] is consistent with initial low degrees of melting in the garnet stability field. A robust result in our modeling is that the conductive heating of the lithosphere is not sufficient to induce large degrees of partial melting in the lithosphere; this, of course, does not rule out the likelihood of various degrees of lithospheric contamination as the magma rises to shallower depths. Certainly the age and the behavior of the lithosphere affect the depth of melting and thus the total melt volume, which

approximately doubles as the initial lithospheric age is reduced from 100 to 20 Ma.

The most important increase in melt volume (up to 1 order of magnitude) is obtained for the case in which lithospheric extension is allowed. However, given the geometry of our model, the melt volumes obtained under radial free-slip boundary conditions represent upper bounds, possibly obtained when a mantle plume is in the proximity of a ridge triple junction. We suggest that variations in the degree of lithospheric extension may be reflected in the differences between the melt volumes produced in continental flood basalts and in oceanic plateaus. The melt volumes of continental flood basalt provinces, though difficult to reconstruct because of erosion, are of order $1-2 \times 10^6$ km³ (but perhaps as high as $6-8 \times 10^6$ km³ if intrusive rocks are considered). Oceanic plateaus show a great variability, the estimated volume for the Kerguelen Plateau is $9-15 \times 10^6$ km³ (if Broken Ridge is included, the total volume is $\sim 15-24 \times 10^6$ km³), and the volume of the Ontong Java Plateau is $\sim 30-60 \times 10^6$ km³ [see *Coffin and Eldholm,* 1994]. We speculate that such volume variations could result entirely from differences in the age and behavior of the lithosphere, rather than differences in plume characteristics. The Kerguelen Plateau probably formed in a new ocean basin, in close proximity to rifting continental lithosphere, just after the breakup between Indo-Madagascar from Antarctica-Australia [e.g., *Storey et al.,* 1992; *Royer and Coffin,* 1992]. The Ontong Java Plateau instead formed in an intraoceanic setting, far away from any sizable continental mass [*Mahoney at al.,* 1993; *Tarduno et al.,* 1991]. A near-ridge hotspot environment satisfies geophysical and geochemical evidence [*Mahoney and Spencer,* 1991], though it can not be confirmed by studies on magnetic anomaly lineations [*Nakanishi et al.,* 1992]. Anyway, the scenario of ridge jumping or a migrating triple junction over a plume head could explain the melt volume and the high degrees of partial melting (~30%) [*Mahoney et al.,* 1993] for the Ontong Java Plateau. For the Shatsky Rise, magnetic lineations indicate that the plateau formed on

oceanic lithosphere along the trace of a triple junction [*Sager and Han*, 1993].

The depth of melting affects the composition of the primary magma, and in our model, melt compositions are rich in MgO. This is a result of the high excess plume temperatures (>300°C) required for sublithospheric melting without extension. The mean MgO concentrations range between 16 and 19 wt %, with the higher values for younger oceanic lithosphere and for higher excess temperatures of the plume head. The relation between the primary magmas at depth and the volcanic products erupted or intruded at shallow depths may be very complicated, and inferences from a simple batch melting model are not entirely satisfactory. However, it is clear that if melting occurs beneath mature lithosphere, the primary magma will have a "picritic-type" composition, so that the erupted tholeiitic basalts are likely derived via crystal fractionation.

The majority of flows in flood basalt provinces are tholeiitic basalts (MgO ~5-8 wt %), and only at the initial and waning stages of volcanism are there differentiated products, from nephelinites to rhyolites. However, the restricted occurrence of picrite basalts (MgO up to 12-16 wt %) is observed in the Karoo [*Cox*, 1972], in the Deccan [*Krishnamurthy and Cox*, 1977], in the North Atlantic Tertiary province [*Clarke*, 1970], and in the Siberian Traps [*Zolotukhin and Al'mukhamedov*, 1988; *Wooden et al.*, 1993]. For the Siberian Traps there is evidence that the parental magma of the entire suite of volcanic products was close in composition to a picritic magma and that the primary process of deep-seated evolution was crystal fractionation [*Zolotukhin and Al'mukhamedov*, 1988; *Wooden et al.*, 1993]. *Krishnamurthy and Cox* [1977] find that the picrite basalts of the Deccan crystallized from ultramafic liquids containing in some cases at least 16 wt % MgO and that the picrites show bulk compositional variation generated by the fractionation of olivine and chromite. Moreover, the evolved picrite basalt magma appears to have given rise to the basalts by the fractionation of olivine and clinopyroxene. For the Karoo the MgO contents of the picrite basalt range from 10 to 24 wt %, with an average close to 15 wt % [*Cox*, 1988]. *Cox and Jamieson* [1974] suggest that the less magnesian-rich picrite basalts have compositions which closely approximate those of the original liquids and that the major element variation of the volcanic products is dominated by the fractionation at high pressure (~10 kbar) of olivine and orthopyroxene.

The composition of the plateaus seems to be predominantly tholeiitic [*Davies et al.*, 1989]; for the Kerguelen Plateau the tholeiites have 4-10 wt % MgO [e.g., *Storey et al.*, 1992], and similar values (MgO 4-9 wt %) generally characterize the Ontong Java basalts [*Mahoney et al.*, 1993]. On the other hand, the volcanic sequence of the oceanic plateaus can be investigated only through drilling, which is limited to the uppermost part of a plateau. An alternative approach to elucidate the deeper crustal levels is through the study of fragments preserved in allochtonous terranes, like Gorgona Island (Colombia), probably a fragment of the Cretaceous Caribbean Plateau [*Storey at al.*, 1991]. The most magnesian-rich flows are komatiites, with MgO up to 24 wt %. Their textural and mineralogical features indicate that they crystallized from superheated liquids, with estimated eruption temperature of order 1500°C, and that the primary magma had an MgO content of ~20 wt % [*Aikten and Echeverría*, 1984].

Petrological evidence thus indicates that at least some primary magmas likely have a picritic composition, possibly with even higher MgO contents in the case of oceanic plateaus [*Storey at al.*, 1991]. However, it is no surprise that the picrites appear only rarely at shallow crustal levels, since their density is higher than either average continental or oceanic upper crust. We suggest that large volumes of crystal cumulates may reside at the crust/mantle interface beneath major flood basalt provinces. They should show up as high-velocity lower crustal layers, and there is, in fact, evidence for such layers beneath the Columbia River Basalt province [*Catchings and Mooney*, 1988] and beneath the Deccan Traps [*Verma and Banerjee*, 1992]. Moreover, refraction experiments on the Kerguelen Plateau [*Charvis and Operto*, 1992] and on Broken Ridge [*Francis and Raitt*, 1967] indicate the presence of a lower crustal body with high seismic velocities (7.3 km/s); similarly, a ~16-km-thick lower crustal body with high seismic velocities (7.4-7.7 km/s), is found in the central Ontong Java Plateau [*Furumoto et al.*, 1976]. This suggests that residual magmas would be tapped episodically from the top of a broad, lenticular magma chamber at the Moho which would be undergoing continual crystal fractionation. We make no attempt here to guess the residence time of such magmas, but there would certainly be opportunity for geochemical interaction with the lower crust and mantle lithosphere. This agrees with *Cox*'s [1980] model for flood basalt volcanism, according to which the uniform composition of the tholeiitic basalts (MgO 4-7 wt %) can be obtained from polybaric evolution of a picritic parent magma (MgO up to 18 wt %). The first phase of crystallization (~25%) is mainly of olivine, and it is followed by the crystallization (another ~25%) of olivine-clinopyroxene-plagioclase at shallower depths, probably in sills intruded at the Moho. *Cox* [1980] concluded that the minimum volume of concealed cumulates can be at least as large as the amount of the erupted surface lavas.

In attempting to model uplift history we have only accounted for thermal buoyancy effects. We have not included specific volume changes due to crystal fractionation or metamorphism in the deep crust [*Falvey and Middleton*, 1981], nor have we included the effect of magmatic underplating [*Cox*, 1989], even though these processes could influence the uplift and subsidence history of a flood basalt province. In general, surface uplift starts at least 10-20 m.y. prior to the expected volcanic activity. Regardless of the mantle viscosity structure we have found that the time sequence of dynamic uplift, subsidence, and volcanic activity occurs over an area within a radial distance of ~350-400 km from the plume axis. At greater distances the uplift phase is induced mainly by the sublithospheric spreading of the plume head, and it may be synchronous with the volcanic activity. For many flood basalt provinces there is growing geological evidence that uplift started at least several million years before volcanism, although it is generally difficult to quantify uplift for continental flood basalt events. For the Karoo and the Deccan [*Cox*, 1989, and references therein] and for the Paraná [*Piccirillo et al.*, 1988] the stratigraphic sequence and geomorphological evidence indicate the progressive change from marine to subaereal conditions over broad areas before flood volcanism. In the Siberian Traps, doming and the formation of arch structures preceded volcanism [*Zolotukhin and Al'mukhamedov*, 1988]. Postvolcanic evolution is generally characterized by subsidence, but as pointed out by *Cox* [1988], provinces such as Deccan, Paraná, and Karoo show evidence of postvolcanic uplift, so that uplift and erosion appear to be long-lived and continuing phenomena in

these areas. *Cox* [1988] suggested that the pattern of highlands may simply be a map of the zones of maximum magmatic underplating or that the dynamics of such areas is further complicated by the subsequent evolution of the continental margins. For the oceanic plateaus it is difficult to reconstruct the sequence of prevolcanic and postvolcanic events since the plateaus are presently submerged, but subsidence analysis indicates that at least part of the Ontong Java Plateau was emplaced in shallow water conditions [*Tarduno*, 1991], while the Kerguelen Plateau eruptions were apparently subaerial, with subsidence below sea level occurring up to 40 m.y. after the cessation of volcanism [*Coffin*, 1992].

Our models, which are constrained to produce at least several million cubic kilometers of melt beneath unrifted lithosphere, predict rather large uplifts of order 2-4 km, depending on whether the environment is continental or oceanic. Perhaps the most detailed evidence for uplift accompanying an oceanic flood basalt province is found in the Triassic strata of the well-known Wrangellia terrane of SE Alaska and British Columbia [*Jones et al.*, 1977]. Wrangellia is an accreted oceanic plateau containing a 3-6 km thick tholeiitic flood basalt, sandwiched between Triassic strata that record the entire uplift/subsidence history of the province. The largely subaerial flood basalts were erupted in at most a few million years and were followed by gradual thermal subsidence of the plateau. Events preceding flood volcanism include rapid emergence from conditions of deep, open ocean (chert) deposition, as well as several less-pronounced, perhaps locally varying, subsidence and uplift events just prior to eruption. The magnitude of uplift is inferred to be of the order of several kilometers. There is no evidence of significant crustal extension accompanying any of these events. This sequence of events is in excellent agreement with the "nonrifting" models developed here, and we have previously suggested that Wrangellia is an almost ideal example of flood volcanism due to a new mantle plume impinging on old oceanic (actually, extinct island arc) lithosphere [*Richards et al.*, 1991]. Our models cannot address the complexity of the crustal/mantle structure under a volcanic arc, but the likely presence of volatiles would certainly enhance melting without substantially changing the time evolution of uplift and melting.

A related and long-debated problem is the relation between flood volcanism and continental break-up. As we already pointed out, some flood basalt provinces (e.g., the Siberian Traps, the Columbia River basalts, and a major event of the Karoo at 193 Ma) were not associated with the opening of a new ocean or with major extension. For other provinces, which are associated with continental rifting, there is often geological evidence suggesting that the volcanism predates the major extension. This is the case for the Paraná [*Piccirillo et al.*, 1988], as shown by recent high-precision radiometric dating [*Renne et al.*, 1992] which indicates that the volcanism predated the opening of the South Atlantic by ~5 m.y. On the other hand, lithospheric uplift caused by the thermal diapir results in horizontal deviatoric stress, and such extensional stresses may at times be sufficient to induce continental extension. *Hill* [1991] and *Houseman and England* [1986] conclude that uplift of ~1-2 km of continental lithosphere is insufficient to provide the driving force for continental break-up, even if it may produce sufficient gravitational potential to induce a local tectonic reorganization. We find that extensional stresses are modest and that the maximum deviatoric stress occurs well before the maximum melt

production. However, some thermal weakening must occur, especially after melt intrusion, and this may facilitate extension during volcanism. The particular regional lithospheric response to the arrival of a new plume will depend on the nature of the lithosphere itself, other plate tectonic forces acting on it at the time, and perhaps also the motion of the lithosphere with respect to the plume.

The great variability of geological circumstances attendant to flood volcanism attests to the fact that interaction between a thermal plume and the lithosphere is very complex, and our simple model must surely be inadequate after the onset of melting. We have ignored the physics of magma migration, as well as many effects of temperature and pressure in the melting zone. Axisymmetric geometry does not allow us to investigate the effects of unidirectional rifting over a plume or the development of small-scale convective instabilities within the plume as it spreads beneath the lithosphere [*Griffiths and Campbell*, 1991]. A fully 3-D model could treat these problems, and it would also be possible to calculate the effects of external forces (i.e., those driving plate motions) or preexisting zones of weakness in the lithosphere.

Perhaps our most significant assumptions involve the melting model itself, and implementation of a more realistic melting scheme could yield important new insights. A fractional or Rayleigh melting scheme would allow us to calculate how the composition of the residuum varies as melting progresses. In this case the melt fraction would be a function not only of the pressure and temperature (as used in the batch melting model) but also of the evolving bulk composition of the residual matrix.

The melting model we have used is anhydrous, and small amounts of water in the mantle can lower the peridotite solidus by several hundred degrees [*Bonatti*, 1990; *Jaques and Green*, 1980]. A compelling case has been made recently by *Gallagher and Hawkesworth* [1992] for the potential importance of water in the mantle lithosphere, and they suggest that flood basalts may be generated by the melting of hydrous phases in the lower continental lithosphere due to impingement of a mantle plume. Obviously, our results do not address this petrological model, and we hope to include models for hydrous melting in future work. However, our focus here has been on plume interaction with a model oceanic lithosphere, and it seems unlikely that the oceanic mantle lithosphere, having been depleted by extensive partial melting at a mid-ocean ridge, would retain a significant volatile content. The high plume temperatures we infer from modeling of sublithospheric, anhydrous melting in the absence of extension represent, as we said at the start, an end-member result from perhaps the simplest geologically relevant case.

References

Aitken, B. G., and L. M. Echeverría, Petrology and geochemistry of komatiites and tholeiites from Gorgona Island, Colombia, *Contrib. Mineral. Petrol.*, 86, 94-105, 1984.

Arndt, N. T., and U. Christensen, The role of lithospheric mantle in continental flood volcanism: Thermal and geochemical constraints, *J. Geophys. Res.*, *97*, 10,967-10,981, 1992.

Bonatti, E., Not so hot "hot spots" in the oceanic mantle, *Science*, *250*, 107-111, 1990.

Brooks, A. N., and T. J. R. Hughes, Streamline upwind/Petrov-Galerkin formulations for convection dominated flows with particular emphasis on the incompressible Navier-Stokes equations, *Comput. Methods Appl. Mech. Eng.*, *32*, 199-259, 1982.

Campbell, I. H., and R. W. Griffiths, Implications of mantle plume structure for the evolution of flood basalts, *Earth Planet. Sci. Lett.*, *99*, 79-93, 1990.

Catchings, R. D., and W. D. Mooney, Crustal structure of the Columbia Plateau: Evidence for continental rifting, *J. Geophys. Res.*, *93*, 459-474, 1988.

Charvis, P., and S. Operto, Variations in the crustal structure beneath the Kerguelen Plateau, *Eos Trans. AGU*, *73*, (43), Fall Meeting suppl., 532, 1992.

Clarke, D. B., Tertiary basalts of Baffin Bay: Possible primary magma from the mantle, *Contrib. Mineral.Petrol.*, *25*, 203-224, 1970.

Coffin, M. F., Emplacement and subsidence of Indian Ocean plateaus and submarine ridges, in *Synthesis of Results from Scientific Drilling in the Indian Ocean*, AGU Monogr. Ser., vol. 70, edited by R. A. Duncan, et al., pp. 115-125, AGU, Washington, D. C., 1992.

Coffin, M. F., and O. Eldholm, Scratching the surface: Estimating dimensions of large igneous provinces, *Geology*, *21*, 515-518, 1993.

Coffin, M. F., and O. Eldholm, Large igneous provinces: Crustal structure, dimensions, and external consequences, *Rev. Geophys.*, *32*, 1-36, 1994.

Cox, K. G., The Karoo volcanic cycle, *J. Geol. Soc. London*, *128*, 311-336, 1972.

Cox, K. G., A model for flood basalt vulcanism, *J. Petrol.*, *21*, 629-650, 1980.

Cox, K. G., The Karoo Province, in *Continental Flood Basalts*, edited by J. D. Macdougall, Kluwer Academic, Norwell, Mass., pp. 239-271, 1988.

Cox, K. G., The role of mantle plumes in the development of continental drainage patterns, *Nature*, *342*, 873-877, 1989.

Cox, K. G., and B. G. Jamieson, The olivine-rich lavas of Nuanetsi: A study of polybaric magmatic evolution, *J. Petrol.*, *15*, 269-301, 1974.

Davies, H. L., et al., Basalt basement from the Kerguelen Plateau and the trail of a Dupal plume, *Contrib. Mineral. Petrol.*, *103*, 457-469, 1989.

Duncan, R. A., and M. A. Richards, Hotspots, mantle plumes, flood basalts, and true polar wander, *Rev. Geophys.*, *29*, 31-50, 1991.

Dziewonski, A. M., and D. L. Anderson, Preliminary Reference Earth Model, *Phys. Earth Planet. Inter.*, *25*, 297-356, 1981.

Falvey, D. A., and M. F. Middleton, Passive continental margins: Evidence for a prebreakup deep crustal methamorphic subsidence mechanism, *Proc. Int. Geol. Congr.*, 26th, 103-114, 1981.

Francis, T. J. G., and R. W. Raitt, Seismic refraction measurements in the southern Indian Ocean, *J. Geophys. Res.*, *72*, 3015-3041, 1967.

Furumoto, A. S., J. P. Webb, M. E. Odegard, and D. M. Hussong, Seismic studies on the Ontong Java Plateau, 1990, *Tectonophysics*, *34*, 71-90, 1976.

Gallagher, K., and C. Hawkesworth, Dehydration melting and the generation of continental flood basalts, *Nature*, *358*, 57-59, 1992.

Griffiths, R. G., and I. H. Campbell, Stirring and structure in mantle starting plumes, *Earth Planet. Sci. Lett.*, *99*, 66-78, 1990.

Griffiths, R. G., and I. H. Campbell, Interaction of mantle plume heads with the Earth's surface, and onset of small-scale convection, *J. Geophys. Res.*, *96*, 18,295-18,310, 1991.

Hager, B. H., Subducted slabs and the geoid: Constraints on mantle rheology and flow, *J. Geophys. Res.*, *89*, 6003-6015, 1984.

Heaman, L. M., A. N. LeCheminant, and R. H. Rainbird, Nature and timing of Franklin igneous events, Canada: Implications for a late Proterozoic mantle plume and the break-up of Laurentia, *Earth Planet. Sci. Lett.*, *109*, 117-131, 1992.

Hill, R. I., Starting plumes and continental break-up, *Earth Planet. Sci. Lett.*, *104*, 398-416, 1991.

Hill, R. I., I. H. Campbell, G. F. Davies, and R. W. Griffiths, Mantle plumes and continental tectonics, *Science*, *256*, 186-193, 1992.

Hooper, P. R., The timing of crustal extension and the eruption of continental flood basalts, *Nature*, *345*, 246-249, 1990.

Houseman, G., and P. England, A dynamical model of lithosphere extension and sedimentary basin formation, *J. Geophys. Res.*, *91*, 719-729, 1986.

Hughes, T. J. R., Generalisation of selective integration procedures to anisotropic and nonlinear media, *Int. J. Numer. Methods Eng.*, *15*, 1413-1418, 1980.

Hughes, T. J. R., *The Finite Element Method*, 631 pp., Prentice-Hall, Englewood Cliffs, N. J., 1987.

Hughes, T J. R., W. K. Liu, and A. Brooks, Finite element analysis of incompressible viscous flows by the penalty function formulation, *J. Comput. Phys.*, *30*, 1-60, 1979.

Jaques, D. F., and D. H. Green, Anhydrous melting of peridotite at 0-15 Kb pressure and the genesis of tholeiitic basalts, *Contrib. Mineral. Petrol.*, *73*, 287-310, 1980.

Jones, D. L., N. J. Silberling, and J. Hillouse, Wrangellia: A displaced terrane in Northwestern North America, *Can. J. Earth Sci.*, *14*, 2565-2577, 1977.

King, S. D., A. Raefsky, and B. H. Hager, ConMan: Vectorizing a finite element code for incompressible two-dimensional convection in the Earth's mantle, *Phys. Earth Planet. Inter.*, *59*, 195-207, 1990.

Krishnamurthy, P., and K. G. Cox, Picrite basalts and related lavas from the Deccan Traps of western India, *Contrib. Mineral. Petrol.*, *62*, 53-75, 1977.

Mahoney, J. J., and K. J. Spencer, Isotopic evidence for the origin of the Manihiki and Ontong Java Plateaus, *Earth Planet. Sci. Lett.*, *104*, 196-210, 1991.

Mahoney, J. J., M. Storey, R. A. Duncan, K. J. Spencer, and M. Pringle, Geochemistry and geochronology of Leg 130 basement lavas: Nature and origin of the Ontong Java Plateau, *Proc. Ocean Drill. Program Sci. Results*, *130*, 3-22, 1993.

McKenzie, D. P., The generation and compaction of partially molten rock, *J. Petrol.*, *25*, 713-765, 1984.

McKenzie, D. P., and M. J. Bickle, The volume and composition of melt generated by extension of the lithosphere, *J. Petrol.*, *29*, 625-679, 1988.

Morgan, W. J., Plate motions and deep mantle convection, *Mem. Geol. Soc. Am.*, *132*, 7-22, 1972.

Morgan, W. J., Hotspot tracks and the opening of the Atlantic and Indian Oceans, in *The Sea*, vol. 7, *The Oceanic Lithosphere*, edited by C. Emiliani, pp. 443-487, John Wiley, New York, 1981.

Nakada, M., and K. Lambeck, Late Pleistocene and Holocene sea-level change in the Australian region and mantle rheology, *Geophys. J. Int.*, *96*, 497-517, 1990.

Nakanishi, M., K. Tamaki, and K. Kobayashi, Magnetic anomaly lineations from late Jurassic to Early Cretaceous in the west-central Pacific Ocean, *Geophys. J. Int.*, *109*, 701-719, 1992.

Olson, P., and I. S. Nam, Formation of seafloor swells by mantle plumes, *J. Geophys. Res.*, *91*, 7181-7191, 1986.

Parson, B., and J. G. Sclater, An Analysis of the variation of ocean floor bathymetry and heat flow with age, *J. Geophys. Res.*, *82*, 803-827, 1977.

Piccirillo, E. M., et al., Continental flood volcanism for the Paraná basin (Brazil), in *Continental Flood Basalts*, edited by J. D. Macdougall, pp. 195-238, Kluwer Academic Norwell, Mass., 1988.

Renne, P. R., et al., The age of the Paraná flood volcanism, rifting of Gondwanaland, and the Jurassic-Cretaceous boundary, *Science*, *258*, 975-979, 1992.

Richards, M. A., Dynamical models for the Earth's geiod, Ph.D. thesis, Calif. Inst. of Technol., Pasadena, 1986.

Richards, M.A., B. H. Hager, and N. H. Sleep, Dynamically supported geoids highs over hotspots: Observation and theory, *J. Geophys. Res.*, *93*, 7690-7708, 1988.

Richards, M. A., R. A. Duncan, and V. E. Courtillot, Flood basalts and hotspot tracks : Plume heads and tails, *Science*, *246*, 103-107, 1989.

Richards, M. A., D. L. Jones, R. A. Duncan, and D. J. DePaolo, A mantle plume initiation model for the Wrangellia flood basalt and other oceanic plateaus, *Science*, *254*, 263-267, 1991.

Royer, J.-Y., and M. F. Coffin, Jurassic to Eocene plate tectonic reconstructions in the Kerguelen Plateau region, *Proc. Ocean Drill. Program Sci. Results, 120,* 917-928, 1992.

Sager, W. W., and H.-C. Han, Rapid formation of the Shatsky Rise oceanic plateau inferred from its magnetic anomaly, *Nature, 364,* 610-613, 1993.

Salters, V. J. M., M. Storey, J. H. Sevigny, and H. Whitechurch, Trace element and isotopic characteristics of Kerguelen-Heard Plateau basalts, *Proc. Ocean Drill. Program Sci. Results, 120,* 55-62, 1992.

Sleep, N. H., Hotspot and mantle plumes: Some phenomonology, *J. Geophys. Res., 95,* 6715-6736, 1990.

Storey, M., J. J. Mahoney, L. W. Kroenke, and A. D. Saunders, Are oceanic plateaus sites of komatiite formation? *Geology, 19,* 376-379, 1991.

Storey, M., et al., Lower Cretaceous volcanic rocks on continental margins and their relationship to the Kerguelen Plateau, *Proc. Ocean Drill. Program Sci. Results, 120,* 33-53, 1992.

Tarduno, J. A., et al., Rapid formation of Ontong Java Plateau by Aptian mantle plume volcanism, *Science, 254,* 399-403, 1991.

Verma, R. K., and P. Banerjee, Nature of continental crust along the Narmada-Son Lineament inferred from gravity and deep seismic sounding data, *Tectonophysics, 202,* 375-397, 1992.

Watson, S., and D. P. McKenzie, Melt generation by plumes: A study of Hawaiian volcanism, *J. Petrol., 12,* 501-537, 1991.

White, R. S., and D. P. McKenzie, Magmatism at rift zones: The generation of volcanic continental margins and flood basalts, *J. Geophys. Res., 94,* 7685-7729, 1989.

White, R. S., D. P. McKenzie, and K. O'Nions, Oceanic crustal thickness from seismic measurements and rare earth element inversions, *J. Geophys. Res., 97,* 19,683-19,715, 1992.

Whitehead, J. A., and D. S. Luther, Dynamics of laboratory diapir and plume models, *J. Geophys. Res., 80,* 705-717, 1975.

Wooden, J. L., et al., Isotopic and trace-element constraints on mantle and crustal contributions to Siberian continental flood basalts, Norilsk area, Siberia, *Geochim. Cosmochim. Acta, 57,* 3677-3704, 1993.

Wyllie, P. J., Solidus curves, mantle plumes and magma generation beneath Hawaii, *J. Geophys. Res. 93,* 4171-4181, 1988.

Zolotukhin, V. V., and A. I. Al'mukhamedov, Traps of the Siberian platform, in *Continental Flood Basalts,* edited by J. D. Macdougall, pp. 273-310, Kluwer Academic, Norwell, Mass., 1988.

C. G. Farnetani, Department of Geology and Geophysics, University of California, Berkeley, CA 94720.

M. A. Richards, Department of Geology and Geophysics, University of California, Berkeley, CA 94720.